4

Elements and Basic Combinations

4.1 Wavelength-Division Multiplexed Frequency Grid

Specification of an internationally recognized standard for the channel frequency locations of a wavelength-division multiplexed optical communication system is essential for component development and system interoperability. Optical components such as signal lasers, multiplexers and demultiplexers, wavelength add-drop filters, and interleavers require a channel location specification to design to.

The current standard for dense wavelength-division multiplexed (DWDM) transmission is specified by the document ITU G694.1 [30]. An anchor frequency of 193.1 THz is defined off of which all other channel locations can be derived. Channel spacings are defined for 12.5 GHz, 25 GHz, 50 GHz, and 100 GHz separations. Figure 4.1 illustrates a partial frequency grid at 100 GHz channel separation. The channel frequency locations f_n are defined as

$$f_n = 193.1 + n \times C \quad \text{(THz)} \tag{4.1.1}$$

where n is a positive or negative integer including zero, and where $C = 0.0125$, $C = 0.025$, $C = 0.050$, or $C = 0.100$. To convert between frequency and wavelength, the value of the speed of light found on page 4 is used by the Standard. Other than the anchor frequency and channel separations there is no adopted standard for how many channels can run on a DWDM system or where those channels are located. The standard is agnostic to implementation.

Nonetheless, there is the practical issue that an optically amplified multispan link requires periodic amplification of the optical signal. An optical amplifier amplifies all channels at once [18]. There are, however, limitations on the bandwidth of the gain due to the physical nature of the rare-earth ions such as erbium that are doped into the optical fiber. There is no single bandwidth that can be attributed to an optical amplifier because the useable bandwidth is governed by both the particular architecture of the amplifier as well as the system application. What is true is that communications carriers who pur-

Jay N. Damask: Polarization Optics in Telecommunications, SSOS 101, 143–210 (2005)

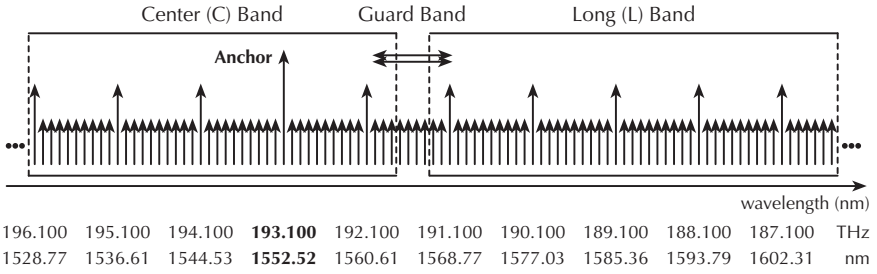

Fig. 4.1. Overview of ITU-T G.694.1 spectral grid for DWDM applications. The anchor frequency is located at 193.100 THz. As illustrated, channel centers are spaced by 100 GHz above and below the anchor frequency. While the Standard is open to higher and lower frequencies than indicated, rough demarcation of center (C) and long (L) bands, with possible intermediate guard band, is shown.

chase the optical transport systems want the lowest overall system cost for the largest aggregate transmission.

There has evolved a banding of the spectrum based on the optical amplifier architectures that are economically manufactured. The C-band, or center band, is the original band where an erbium-doped optical amplifier provides high gain efficiency. This band is often delineated by the range 192.1 to 196.1 THz. The L-band, or long band, is recently available using erbium-doped fiber. That band is often delineated by the range 186.1 to 191.1 THz. These ranges vary from vendor to vendor. Because the C- and L-bands have different gain efficiencies for pumps wavelengths of 1480 or 980 nm, separate amplifiers are built for these each band. A Raman amplifier can pump the entire spectrum seamlessly, however. For diode-pumped systems, a band-separation filter splits the two bands prior to amplification and then combines them prior to transmission. Typically there is a guard band between the C- and L-bands to accommodate the band-separation filter. However, recently demonstrated filter improvements can eliminate the need for a guard band.

There is no standard for the deviation of laser or filter center frequency from the center frequency of the grid [29]. The end-of-life specification depends on many factors, including the maximum foreseeable channel density. For the purposes of analysis in this text, the allowable beginning-of-life frequency deviation will be taken as $\Delta f = \pm 2.5$ GHz.

There are several reasons the definition of the spectral grid is important for component designers. These reasons include

- The tolerance on the FSR of a periodic component must allow for channel alignment across a band.
- The frequency centering of a periodic component with the correct FSR must align to the channel locations.
- The bandwidth of polarization transforming elements such as waveplates must cover a band.

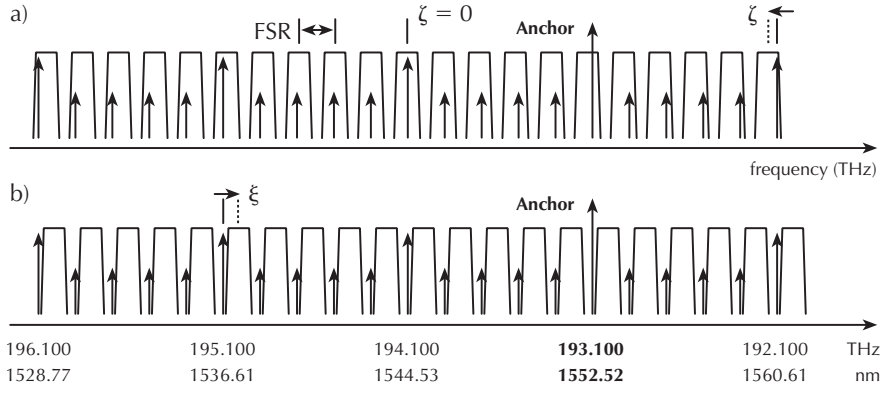

Fig. 4.2. Two types of filter placement errors in relation to the DWDM spectral grid. a) FSR error leads to walkoff between spectral grid and filter centers. While at one frequency the grid and filter may align ($\zeta = 0$) at the band edges the filter is misaligned. b) Frequency location error ξ, often called phase error. Even if the FSR is within tolerance, the filter center frequencies may suffer a common misalignment to the spectral grid.

Figure 4.2 illustrates the first two error types. In Fig. 4.2(a) the FSR of a periodic element such as an interleaver filter is too small, leading to a walkoff over the band. Denote the frequency separation between the grid and the filter at either band end as ζ. The tolerable FSR error of a component is then

$$\frac{\delta\text{FSR}}{C} = \frac{|C - \text{FSR}|}{C} = \frac{|\zeta|}{NC} \tag{4.1.2}$$

where C is the designed channel separation and N is the number of channels between band center and band edge. For example, in a C-band designed with 40 channels on 100 GHz centers, $N = 20$. With the aforementioned filter location tolerance of $\Delta f_n = \pm 2.5$ GHz, the FSR tolerance of the filter is

$$\frac{\delta\text{FSR}}{C} = \frac{|2.5|}{20 \times 100} = 0.125\% \tag{4.1.3}$$

For a resonant element such as a Fabry-Perot, a 0.125% tolerance for a 1 mm long cavity is about one micron. The broader the band coverage the tighter the cavity-length tolerance.

In Fig. 4.2(b) $\delta\text{FSR} = 0$, but there is a common frequency offset error ξ across all the channels. The frequency tolerance is generally more than the FSR tolerance because the error does not accumulate across multiple channels. As such, the frequency tolerance δf is

$$\frac{\delta f}{\text{FSR}} \simeq \frac{|\Delta f|}{C} \tag{4.1.4}$$

As with the preceding example, the frequency tolerance is $\delta f = 2.5\%$ FSR.

In relation to polarization elements and material dispersion, the spectral coverage of the system should be tolerated by the component. For a C-band that covers 192.1 to 196.1 THz, the spectral coverage $\mathcal{S}_C$ of this band is

$$\mathcal{S}_C = \frac{196.1 - 192.1}{194.1} \simeq 2.061\% \tag{4.1.5}$$

Likewise, an L-band that covers 186.1 to 191.1 THz has a spectral coverage $\mathcal{S}_L$ of

$$\mathcal{S}_L = \frac{191.1 - 186.1}{188.6} \simeq 2.651\% \tag{4.1.6}$$

The combined spectral coverage is $\mathcal{S}_{C+L} = 5.23\%$. These are broad coverages for waveplates, Faraday rotators, and anti-reflection coatings to cover. In many cases compromises or increased complexities are required to satisfy these bandwidth demands.

4.2 Properties of Select Materials

A central theme of this text is to provide information necessary to realize the components whose architectures are detailed in subsequent chapters. To this end it is essential to have on hand the physical and optical properties of the relevant materials. This section tabulates the properties of select isotropic optical materials, select birefringent materials, and select metal and alloy materials used for packaging. Faraday rotators made from iron-garnet derivatives are covered at the end. These are not intended to be an exhaustive tabulation but rather a short reference for the commonly used materials.

4.2.1 Isotropic Glass Materials

Isotropic glass materials are used both as optical elements and as packaging and assembly parts. There are a large number of well-characterized glasses available from major suppliers [28, 38, 45]. Principal factors used to select a low-loss glass for optical transmission use include its refractive index at the wavelength of use; the refractive index dispersion; its thermal-optic coefficient, or change of refractive index with temperature; and its thermal-expansion coefficient [44]. The refractive index and its dispersion will govern such attributes such as the angle of a prism made from a particular glass, while the thermal-optic coefficient is necessary to tolerance the component over the required temperature range. The thermal expansion coefficient is important because a package assembled from a variety of materials must maintain its integrity over its lifetime. If one part expands significantly more than the others then adhesion, for example, can be compromised.

Glass parts are sometimes used for packaging and assembly parts as well. Two key factors when choosing such as glass are its thermal expansion coefficient and its ultraviolet (UV) transmissivity. A glass package part is often

Table 4.1. Select Isotropic Glass Materials

Property		Fused silica[a]	N-BK7[b]	**Units**
Density		2.2	2.51	g/cm^3
Hardness		5-6		Mohs
Thermal conductivity		1.31	1.114	W/(m·K)
Thermal expansion		0.5[c]	7.1[d]	$\times 10^{-6}$/K
Refractive index $n_{1529.6}$		1.44424	1.50091	
Thermal optic[e]				
1060 nm line			2.4	$\times 10^{-6}$/K
e-line		9.9	3.0	
Sellmeier coefficients[f]	B1	0.66942	1.03961	λ in μm
	B2	0.43458	0.23179	
	B3	0.87169	1.01047	
	C1	0.00448	0.00600	
	C2	0.01328	0.02002	
	C3	95.3414	103.561	

[a] Reported by Schott [45].

[b] Reported by Schott [46].

[c] 25°C-100°C, [d] -30°C-+70°C, [e] 20°C-40°C, $\Delta n_{\text{rel}}/\Delta T$.

[f] $n^2(\lambda) - 1 = \dfrac{B_1\lambda^2}{\lambda^2 - C_1} + \dfrac{B_2\lambda^2}{\lambda^2 - C_2} + \dfrac{B_3\lambda^2}{\lambda^2 - C_3}$, [45].

used because its thermal expansion matches with other glassy parts that are in the transmission path. Another reason is that the transmission parts need to be visible during assembly, for alignment and/or for UV tacking with epoxy. Finally, glass windows are sometimes brazed into metal packages to make a clear path for collimators while maintaining hermetic integrity.

While a complete glass catalog should be referred to in order to choose an optical glass for a particular application, Table 4.1 provides select material properties of two commonly used transmission and packaging glasses: fused silica and BK7.

4.2.2 Birefringent Crystals

Birefringent crystals are the basic building blocks for the birefringent components detailed in the following chapters. The crystal materials may be divided into two application regimes: applications requiring high birefringence and those requiring low birefringence. Rutile and yttrium orthovanadate (YVO_4) are examples of very high birefringent material, both having about 10% birefringence at 1.55 μm. Crystalline quartz is a readily available low birefringent material, having a birefringence of 0.0084 at 1.55 μm.

Materials of intermediate birefringence are nonetheless required for practical reasons. For example, the birefringent phase of a birefringent crystal is tem-

Prop
Cryst
Biref
Spac
Dens
Hard
Hydr
Latti
Ther
Ther
Refra
Biref
Ther
Grou
Grou
Ther
Sellm

(a) R
(b) R
(s) R
(d) R

Propert
Crystal
Birefring
Space gr
Density
Hardnes
Hydrosc
Lattice
Thermal
Thermal
Thermal
Refracti
Birefring
Optical

[s] Repo

[c] Repo

[d] At λ

perature dependent. But two crystals having complementary thermal-optic coefficients can be cascaded to mitigate the temperature dependence passively. Useful complementary crystals for YVO_4 are $LiNbO_3$ and lead molybdate, both of which have an intermediate birefringence. Alternatively, intermediate birefringent crystals such as $LiNbO_3$ have strong electro-optic coefficients, making them useful for switching and polarization-control applications.

Tables 4.2 and 4.3 provide a compilation of data on nine widely used birefringent materials. All of these materials are synthetic except for calcite, which is found in nature and mined. Because the crystal quality can vary and the material is not sufficiently hydrophobic, calcite is not a favored component-grade material. In comparison with rutile, YVO_4 is favored because it is more easily grown to large boule sizes and is easier to handle at the grinding and polishing stages. To compensate for the temperature dependence of YVO_4, $LiNbO_3$ is commonly used, although lead molybdate has been recently proposed. Tellurium dioxide is a reasonably high birefringent crystal with the added feature that it can be grown in high-purity dextrorotatory and laevorotatory chiralities, enabling the crystal to be used for optical activity. α-BBO is a negative uniaxial crystal that is not commonly used due to its intermediate birefringence, but one interleaver design pairs its negative uniaxial property with the positive uniaxial YVO_4 to make a compound crystal that imparts no Poynting vector walkoff.

Finally, crystalline quartz is extensively used for waveplates because of its high material quality and its low birefringence. The birefringent beat length of quartz is about 184 μm at 1.55 μm wavelength, so a true zero-order half-wave waveplate at this wavelength is 92 μm thick. In contrast, the birefringent beat length of $LiNbO_3$ is about 19 μm; an equivalent half-wave waveplate is 9.5 μm thick, a nearly impossible thickness to reproducibly attain.

4.2.3 Iron Garnets

Faraday rotators (FR) provide the requisite nonreciprocal polarization rotation necessary for isolators and circulators. The optical properties of Faraday rotation were detailed in §3.7.6. Here the material properties and design goals of iron garnet FRs are outlined.

An iron garnet is a ferrimagnetic material that has several orders of magnitude greater rotary power than diamagnetic materials. Practical iron garnets are most commonly grown by the liquid-phase epitaxy. A substrate such as gadolinium gallium garnet (GGG) is used to nucleate the crystalline growth and support the film. After the film is grown, usually to 250–500 μm thick, the substrate is ground away and both sides of the remaining film are polished. Anti-reflection coatings are then applied and the film is diced into square parts, typically 2×2 mm^2.

To use an iron garnet FR, the finished part is placed at the center of a annular permanent magnet such as samarium-cobalt (Sm-Co). The major face of the garnet part is placed in the clear aperture of the permanent magnet and,

Table 4.4. Non-Latching Iron Garnet Design Goals

High specific Faraday rotation	$\theta'_F > 0.1^\circ/\mu$m
Low thickness for $\theta'_F = 45^\circ$	$t < 500$ μm
Low absorption	IL < 0.1 dB
Low saturation magnetization	$H_{\text{sat}} < 400$ Oe
Good substrate lattice matching	match to GGG or like
Low pitting density	$< 10/\text{cm}^2$
Temperature range	-20 to $+70^\circ$C
Low temperature coefficient	$d\lvert\theta'_F\rvert/dT < 0.07^\circ/\text{C}$
Low wavelength dependence	$d\lvert\theta'_F\rvert/d\lambda < 0.08^\circ/\text{nm}$
High Curie temperature	$T_c > 150^\circ$C

accordingly, the magnetization vector within the film is normal to the film surface. The strength of the magnet must be sufficient to saturate fully the domain structure of the garnet over the specified temperature range. Multi-magnet schemes have been proposed to enhance the magnetic field in the region surrounding the magnet [23, 25], although these concepts are not currently used in telecom-grade components. The direction of magnetization sets the direction of polarization rotation, whether clockwise or counterclockwise. Light transits the garnet part either parallel or anti-parallel to the magnetization direction.

To attain component-quality performance, the FR must have a low saturation magnetization H_{sat} so the permanent magnetic can be small, a low absorption, a low temperature-dependent specific rotation (defined by (3.7.38) on page 135), and a low wavelength-dependent specific rotation. Moreover, the film must closely lattice match to the substrate, over the range of room and growth temperatures, to enable crystal growth. The requisite qualities of a telecommunications-grade iron garnet used in isolators and circulators, as opposed to magneto-optic sensor applications, are listed in Table 4.4.

Yttrium iron garnet (YIG) is an early garnet material that was a suitable replacement for diamagnetic FRs of the time. With a chemical formula of $Y_3Fe_5O_{12}$, the iron content is the sole contributor to the magnetization as Y has no net magnetic moment. In relation to the component requirements, however, a YIG film must be ~ 2.7 mm to achieve a rotation of $\theta_F = 45^\circ$. Also, YIG has a large saturation magnetization (~ 1800 G), requiring a large permanent magnet.

To reduce the requisite film thickness, bismuth exchanged rare-earth iron garnets (Bi:RIG) were introduced. With the chemical formula $(\text{BiRE})_3Fe_5O_{12}$, the combined bismuth and rare-earth (RE) ions greatly enhance the specific rotation. There are, however, tradeoffs due to the exchange of (BiRE) for yt-

trium. The bismuth ion increases the lattice constant of the film; it increases the temperature dependence of the specific rotation; it increases the thermal expansion of the film; and it increases the possibility of pitting in the film. The lattice mismatch limits bismuth incorporation to about one atom in three. These deleterious effects may be somewhat compensated by the selection and concentration of the rare-earths. Addition of terbium (Tb), for example, will decrease the temperature dependence. Which rare-earth atoms are suitable depends in large part on their absorption spectra and the operating wavelength of the garnet. At 1.55 μm, Tb, gadolinium (Gd), holmium (Ho), and europium (Eu) are all suitable to varying degrees. However, at 980 nm their absorption is too high and other means, such as heavy bismuth loading and a 25 μm film [21], is all that can be expected.

To reduce the saturation magnetization, gallium and aluminum can be substituted for iron as in $(\mathrm{BiRE})_3(\mathrm{FeGaAl})_5\mathrm{O}_{12}$. Introduction of Ga and/or Al, however, concurrently reduces the Curie temperature (the temperature at which the magnetization is zero) and increases the temperature dependence of the specific rotation.

Very interesting studies have been conducted to tailor the overall material properties through introduction and balancing of rare-earth ions as well as gallium and aluminum. With the optimal balance, there is a window of material compositions in which all of the iron garnet design goals listed in Table 4.4 can be achieved. A single source that presents the various tradeoffs is [21]. The combined patent work of [1, 27, 47–51, 53] provides many practical details about compositions and materials processing.

As a specific example, $(\mathrm{Tb}_{1.69}\mathrm{Bi}_{1.31})(\mathrm{Fe}_{4.38}\mathrm{Ga}_{0.42}\mathrm{Al}_{0.20})\mathrm{O}_{12}$ [27] exhibits $H_{\mathrm{sat}} = 340$ Oe at $+60°$C, $\theta'_F = 0.099°/\mu$m and a temperature dependence of $0.062°$/C. It should be noted that the wavelength dependence of iron garnets is generally small and does not follow Biot's law.

All of the above described iron garnets follow the linear saturation curve of Fig. 3.20. These garnets are non-latching and require the presence of a permanent magnet to maintain alignment of the magnetic domains. Latching garnets, in contrast, require only a one-time poling by a strong magnet and then retain their magnetization indefinitely under normal conditions. A latching garnet is perfectly hysteretic, as illustrated by the latching curve in Fig. 3.20. As a practical matter, once the garnet is poled, proper orientation in a component is critical: reversing the part will create high transmission rather than high isolation. To make the direction of magnetization easy to identify, reference [52] reports the idea of making the AR coating on the two sides of the film different in color. A light purple can be made from a three-layer coating while a bluish purple can be made from a single-layer coating.

A linear hysteresis loop results from the film's natural tendency to fracture into domains rather than remain in a single domain. The magneto-static energy of the film is proportional to the square of the saturation magnetization: a high H_{sat} provides sufficient energy for domain break up. However, doping with Ga and/or Al decreases the saturation magnetization, increasing

Table 4.5. Select Alloy Packaging Materials

Property	Kovar[(a)]	Invar-36[(b)]	**Units**
Element			
Carbon	0.020%	0.020%	
Silicon	0.20%	0.20%	
Cobalt	17%	-	
Manganese	0.30%	0.35%	
Nickel	29.0%	36.0%	
Iron	balance	balance	
Density	8.39	8.09	g/cm^3
Thermal Conductivity	17.3	10.5	W/(m·K)
Thermal Expansion[(c)]	5.85	1.30	cm/cm/K
Electrical Resistivity[(d)]	487	820	$\mu\Omega$-mm
Melting Point	1470	1445	°C

[(a)] Reported by Carpenter [12].
[(b)] Reported by Carpenter [11].
[(c)] 25°C-100°C, [(d)] 70.0°F.

in turn the hysteresis of the material. By lowing H_{sat} to below 100 G, latching can occur. As an example, $(Bi_{0.75}Eu_{1.5}Ho_{0.75})(Fe_{4.1}Ga_{0.9})O_{12}$ has a thickness of 86 μm for 45° rotation and a saturation magnetization of 14 Oe [7]. However, the temperature dependence necessarily increases due to the high Ga concentration. The temperature dependence of the preceding film is reported as −0.093°/C [21].

The latching garnet is perfectly suited for an isolator placed at the output of a diode laser within the hermetic housing [22]. A semiconductor laser diode, used for signal and pump lasers, requires a miniature housing where elimination of the permanent magnet is a significant advantage. To maintain the lasing wavelength, laser diodes sub-mounts are attached to Peltier thermal-electric coolers that maintain the temperature. The latching garnet is also placed on the cooler. Under these conditions the latching garnet performs well. In passive component applications, however, where the garnet must remain stable over a wide temperature range, low temperature-dependent garnets are a better choice.

4.2.4 Packaging Alloys

Packaging materials play an integral role in component design and assembly because they house the optical core and must resist environmental interference. Industry standards such as [58] place stringent conditions on the heat and humidity a component must tolerate over its 25–year lifetime. Generally, telecommunications-grade components require hermetic sealing to protect the optical surfaces and attachment epoxies from heat and humidities. Specialty

components such as air-gap interleavers do a final frequency tuning by adjusting an inert-gas overpressure prior to sealing the package, after which that overpressure is expected to be maintained.

Table 4.5 provides information on two commonly used alloys, Kovar and Invar. These alloys are suitable for their machinability and low thermal expansion coefficient. Typically these alloys are plated with one or two mils thickness nickel and gold, in that order. The nickel promotes the gold adhesion, and the gold prevents corrosion while providing a quality surface on which to solder and weld.

4.3 Fabry-Perot and Gires-Tournois Interferometers

Two elementary components are the Fabry-Perot (FP) and Gires-Tournois (GT) interferometers. Both interferometers are resonators that store energy two partially reflecting mirrors when on resonance between. For the Fabry-Perot, leakage of the stored energy through the partial reflectors interferes constructively (destructively) with the input light to alter the transmission (reflection) properties. By comparison, on anti-resonance there is no energy stored and the transmission is minimum. The Gires-Tournois is also a resonator but with the second mirror fully reflecting. The reflection coefficient is unity but there is a frequency-dependent delay associated with resonance. The response of these two resonators is typically derived using an infinite series construct. Here, scattering and transmission matrices are first derived and then a matrix concatenation is used to reach the solution. In either formalism the final equations are the same, but the transformation matrix approach is applicable to a broader range of calculations.

The first step is to derive a scattering matrix S across an index-step boundary such as a partially reflecting mirror. The matrix relates the outputs across the boundary to the inputs (Fig. 4.3(S)):

$$\begin{pmatrix} b_1 \\ b_2 \end{pmatrix} = \begin{pmatrix} s_1 & s_2 \\ s_3 & s_4 \end{pmatrix} \begin{pmatrix} a_1 \\ a_2 \end{pmatrix} \tag{4.3.1}$$

Since the system is lossless, the scattering matrix must be unitary:

$$S^\dagger S = I \tag{4.3.2}$$

The scattering matrix elements are found from (3.5.31) on page 97. A phase reference plane is established on either side of the boundary. On the side of the reflection, the phase reference is chosen so that $\Gamma/|\Gamma| = +1$, or $2k_{z1}z = 2n\pi$. On the side of transmission, the phase reference is chosen so that $T/|T| = -j$, or $k_{z2}z = (2n - 1/2)\pi$. One can say that for a given wavelength the phase reference plane for reflection coincides with the boundary surface and the phase reference plane for transmission is set back by a quarter-wave on the far

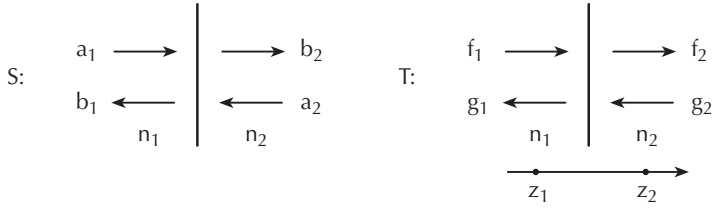

Fig. 4.3. Scattering and transmission coefficients across an index-step boundary. S) Scattering coefficients, inputs denoted by a, outputs denotes by b. T) Transmission coefficients, forward waves denoted by f, backward waves denoted by g.

side of the boundary. With these definitions and enforcing the unitary property of the scattering matrix, the scattering matrix of a partially transmissive mirror are

$$S = \begin{pmatrix} r & -jt \\ -jt & r \end{pmatrix} \tag{4.3.3}$$

where r and t are the reflection and transmission field amplitudes, respectively. The reflection and transmission coefficient related by

$$r^2 + t^2 = 1 \tag{4.3.4}$$

ensures a lossless interface. The physical interpretation of the $-j$ multiplier to the transmission coefficient is that the passage of a wave across the boundary is delayed by $\pi/2$ with respect to a wave reflected.

Next the scattering matrix is converted to a transformation matrix. The latter matrix relates the forward and backward waves at one location z_1 to the forward and backward waves at another location z_2 (Fig. 4.3(T)). A transformation matrix can be concatenated with other transmission matrices to find the response of a more complicated system. This is not the case for the scattering matrix, which is the reason for the conversion. In regard to the figure, the field amplitudes of the scattering and transformation frameworks are related in the following way:

$$\begin{aligned} f_1 &= a_1, \qquad f_2 = b_2, \\ g_1 &= b_1, \qquad g_2 = a_2. \end{aligned}$$

The field amplitudes are related to the transformation matrix as

$$\begin{pmatrix} f_1 \\ g_1 \end{pmatrix} = \begin{pmatrix} t_1 & t_2 \\ t_3 & t_4 \end{pmatrix} \begin{pmatrix} f_2 \\ g_2 \end{pmatrix} \tag{4.3.5}$$

The transformation matrix for the partially transmissive mirror is therefore

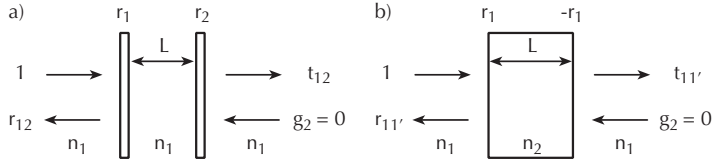

Fig. 4.4. Fabry-Perot interferometers with planar partially reflective mirrors. a) Two mirrors with reflectivities r_1 and r_2 separated by distance L. b) Model of a solid of index n with equal magnitude Fresnel reflections on either face. One reflection is the negative of the other.

$$T(z_1, z_2) = \frac{j}{t} \begin{pmatrix} 1 & -r \\ r & -1 \end{pmatrix} \tag{4.3.6}$$

Note that the determinant of (4.3.6) is $\det(T) = -jt$; reflection appears as loss to the forward-going waves.

A Fabry-Perot is modelled with two partially reflecting mirrors separated by gap L. Free propagation to position z' from z, where $z' > z$, is simply

$$T(z', z) = \begin{pmatrix} \mathrm{e}^{-jkL} & 0 \\ 0 & \mathrm{e}^{jkL} \end{pmatrix} \tag{4.3.7}$$

where the wavenumber k is given by the dispersion relationship $k = \omega nL/c$. Two Fabry-Perots are illustrated in Fig. 4.4, one with an air gap and the other made of a solid block.

An important simplification for finding the transmission and reflection coefficients of the FP is to null one input, in this case $g_2 = 0$ as illustrated in Fig. 4.4. The transmission and reflection amplitudes t_{12} and r_{12}, respectively, are then determined from $t_{12} = f_2/f_1$ and $r_{12} = g_1/f_1$. The left- and right-hand sides are related by the FP transformation matrix

$$T_{\mathrm{fp}}(z_1, z_2) = -\frac{1}{t_1 t_2} \begin{pmatrix} 1 & -r_1 \\ r_1 & -1 \end{pmatrix} \begin{pmatrix} \mathrm{e}^{-jkL} & 0 \\ 0 & \mathrm{e}^{jkL} \end{pmatrix} \begin{pmatrix} 1 & -r_2 \\ r_2 & -1 \end{pmatrix} \tag{4.3.8}$$

Expansion of (4.3.8) and identification of terms leads to

$$t_{12} = -\frac{t_1 t_2}{\mathrm{e}^{-jkL} - r_1 r_2 \mathrm{e}^{jkL}} \tag{4.3.9a}$$

$$r_{12} = +\frac{r_1 \mathrm{e}^{-jkL} - r_2 \mathrm{e}^{jkL}}{\mathrm{e}^{-jkL} - r_1 r_2 \mathrm{e}^{jkL}} \tag{4.3.9b}$$

The transmitted and reflected powers are the squared-magnitudes of the preceding expressions.

4.3.1 Fabry-Perot Response

The general transmission and reflection coefficients for a Fabry-Perot are given by (4.3.9). Two special cases are considered here.

For the first special case, $r_1 = r_2 = r$. The power coefficients are

$$|t_{11}|^2 = \frac{(1-R)^2}{1+R^2-2R\cos(2kL)} \tag{4.3.10a}$$

$$|r_{11}|^2 = \frac{2R\,(1-\cos(2kL))}{1+R^2-2R\cos(2kL)} \tag{4.3.10b}$$

where $R = r^2$, $T = t^2$, $R + T = 1$, and coefficient T and transformation matrix T are distinguished by context.

For the second special case, illustrated in Fig. 4.4(b), the reflection coefficients on the two boundaries have opposite sign: $r_2 = -r_1$. The power transmitted is

$$|t_{11'}|^2 = \frac{(1-R)^2}{1+R^2+2R\cos(2kL)} \tag{4.3.11}$$

where the effect of the negative second reflection coefficient is to shift the transmission (and reflection) spectrum by a half period as compared with (4.3.10). An exemplar transmission spectrum is illustrated in Fig. 4.5, where the FP interferometer is a solid block.

The transmission spectrum of a Fabry-Perot is periodic and depends on the phase accumulation in the resonator. The transmission is related to the resonator phase as

$$|t_{11}|^2 = \begin{cases} 1 & \text{resonance: } 2kL = 2n\pi, \\ \dfrac{(1-R)^2}{(1+R)^2} & \text{anti-resonance: } 2kL = (2n+1)\pi \end{cases} \tag{4.3.12}$$

Of course, if there is loss in the system then the transmission maximum is less than unity. Also, the conditions for resonance and anti-resonance for the solid-block FP are switched from those in (4.3.12).

In general, a modulation depth MD is defined as

$$\mathrm{MD} = \frac{I_{\max} - I_{\min}}{I_{\max} + I_{\min}} \tag{4.3.13}$$

where I is intensity. Substitution of (4.3.12) into (4.3.13) gives the modulation depth for a Fabry-Perot interferometer:

$$\mathrm{MD}_{\mathrm{FP}} = \frac{2R}{1+R^2} \tag{4.3.14}$$

The range of modulation depth is from zero to unity and is governed solely by the mirror reflectivity R.

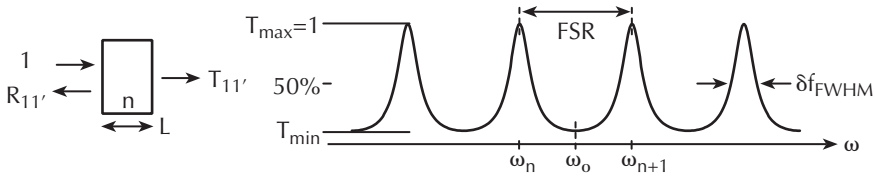

Fig. 4.5. Solid Fabry-Perot interferometer; the second reflection coefficient is the opposite sign of the first. For a unit input there is frequency-dependent transmission and reflection. Left: exemplar transmission spectrum for solid FP. A comb of transmission peaks exists in frequency, spaced by the free-spectral range (FSR) of the cavity. The modulation depth is governed solely by the boundary reflectivity.

Free-Spectral Range and Group Index

As illustrated in Fig. 4.5 the transmission (and reflection) spectrum is periodic. The periodic structure is dictated by the resonator phase $\phi = 2kL$. The free-spectral range (FSR) of the interferometer is defined as the frequency shift required to offset the spectrum by one full period. That is, the change in phase must be $\Delta\phi = 2\pi$. Expanding the phase to show radial frequency ω,

$$\phi = 2\frac{\omega}{c}\, n(\omega)L \tag{4.3.15}$$

the phase difference is related to the frequency difference by

$$\begin{aligned}\Delta\phi &= \frac{2L}{c}\left(\omega_2 n(\omega_2) - \omega_1 n(\omega_1)\right) \\ &= \frac{2L}{c}\,\Delta(\omega n(\omega))\end{aligned} \tag{4.3.16}$$

The difference on the right-hand right may be written

$$\begin{aligned}\Delta(\omega n(\omega)) &= \frac{d(\omega n(\omega))}{d\omega}\Delta\omega \\ &= \left(n + \omega\frac{dn}{d\omega}\right)\Delta\omega\end{aligned} \tag{4.3.17}$$

After the more customary conversion to wavelength from frequency, the group index is defined as

$$n_{\rm g} = n - \lambda\frac{dn}{d\lambda} \tag{4.3.18}$$

Substitution of (4.3.17-4.3.18) into (4.3.16) and conversion to cycle frequency from radial frequency yields

$$\Delta\phi = 2\pi\frac{2n_{\rm g}L}{c}\,\Delta f \tag{4.3.19}$$

The free-spectral range FSR $= \Delta f$ is defined for $\Delta\phi = 2\pi$, or

$$\mathrm{FSR} = \frac{c}{2n_g L} \tag{4.3.20}$$

That the FSR is defined by the group index is a statement that it is the round-trip time of the optical energy, and not phase, that matters. The difference between phase and group index is critically important when building precision instruments such as optical clocks, where the phase and group velocities in an resonant cavity must be locked [33, 37]. Optical fibers also exhibit a difference between phase and group indices, a difference that varies from unspun to spun fibers, across vintages, and across fiber types [36].

Resonant Bandwidth

Also illustrated in Fig. 4.5 is the full-width half-maximum δf_{FWHM} of the transmission spectrum. For a symmetric lossless Fabry-Perot, as long as the mirror reflectivity exceeds

$$R \geq \frac{\sqrt{2}-1}{\sqrt{2}+1} \tag{4.3.21}$$

then the transmission will fall below 50%. Setting (4.3.10) to 50% and solving for the resonant bandwidth δf_{FWHM} yields

$$\delta f_{\mathrm{FWHM}} = \frac{2}{\pi}\,\mathrm{FSR}\sin^{-1}\frac{1-R}{2\sqrt{R}} \tag{4.3.22}$$

In the highly resonant case, where $\delta\phi_{\mathrm{FWHM}} \ll \pi$, then

$$\delta f_{\mathrm{FWHM}} \simeq \frac{1-R}{\pi\sqrt{R}}\,\mathrm{FSR} \tag{4.3.23}$$

Fabry-Perot interferometers are classically used as narrowband filters because the transmission on resonance is unity and a high mirror reflectivity makes the resonant bandwidth narrow. For practical applications, FP filters are not good wavelength-division multiplexing filters unless they are cascaded to make a multi-pole filter with higher roll off and flatter transmission profiles. The FP resonator is sometimes used, however, as a frequency standard on which to lock a transmission laser frequency.

Tolerancing the Resonance Frequency

The following tolerance analysis illustrates the necessary specifications for a telecommunications-grade Fabry-Perot interferometer. Consider a FP etalon made of BK7 glass that nominally aligns its transmission spectrum to a DWDM grid of $C = 100$ GHz in the C-band. The frequency-dependent argument $(2kL)$ of the transmission expression (4.3.11) nominally aligns to the DWDM comb of frequencies f_n:

$$2\pi f_n \frac{2n_g L}{c} = (2n+1)\pi \tag{4.3.24}$$

Nominally FSR $= C$, so

$$f_n = \left(n + \frac{1}{2}\right) C \tag{4.3.25}$$

Due to errors, however, the free-spectral range may have an error. That error requires an offset from f_n to reach the nominal frequency comb f_n. That is,

$$2\pi \frac{f_n \pm \delta f}{\text{FSR} \pm \delta\text{FSR}} = 2\pi \frac{f_n}{C} \tag{4.3.26}$$

Substitution of the nominal grid (4.3.25) into (4.3.26) gives the error proportionality

$$\frac{\delta\text{FSR}}{C} = \frac{\delta f}{f_n} \tag{4.3.27}$$

Using the specification in §4.1 of $\Delta f_n = \pm 2.5$ GHz and a center frequency of $f_n = 194.1$ THz, the allowable error on the free-spectral range is

$$\left|\frac{\delta\text{FSR}}{C}\right| \leq 13 \text{ ppm} \tag{4.3.28}$$

This error tolerance is almost impossibly small.

To relax the tolerance one can separate the frequency-location error from the FSR error. That is, rather than insisting the FSR exactly match the grid exactly, the FSR is allowed to walkoff the grid over some bandwidth. This is illustrated in Fig. 4.2(a). The calculation made in (4.1.3) gives a 1250 ppm error tolerance to the FSR.

Separate from the FSR accuracy, the resonant peaks must still align to the grid. At center frequency the number of modes in the cavity is $n \simeq 1941$. The length of BK7 to realize the cavity, using round numbers, is $L = 1.000$ mm. As there are 1941 modes in the cavity, the mode length is $l = 0.515$ μm. A change in cavity length by 0.515 μm times an integral number adds or removes modes to the cavity, but a non-integral length change shifts the frequency location of the resonant peaks. Using the frequency-error tolerance $\Delta f_n = \pm 2.5$ GHz, any change in cavity index-length product must be within

$$\left|\frac{\delta(n_g L)}{n}\right| \leq \frac{1.5}{1941} \times 2.5\% \tag{4.3.29}$$

or

$$|\delta(n_g l)| \leq 0.020 \ \mu\text{m} \tag{4.3.30}$$

Expansion of the index-length product to account for temperature dependence gives

$$\delta(n_g l) = n_g \Delta T \frac{dl}{dT} + l \Delta T \frac{dn_g}{dT} \tag{4.3.31}$$

Using the thermal expansion and thermal optic coefficients for BK7 found in Table 4.1 and accounting for a ±50°C temperature swing, the error budget due to temperature change is

$$n_{\mathrm{g}}\Delta T\frac{dl}{dT}+l\Delta T\frac{dn_{\mathrm{g}}}{dT}\simeq 0.683\ \mu\mathrm{m} \tag{4.3.32}$$

In comparison with (4.3.30) one can clearly see that a bulk Fabry-Perot cavity does not meet the tolerance requirements for a telecommunications component. These cavities require active temperature control to meet the necessary specifications. In practice, the cavities are made with an air gap sealed hermetically into a package, and the construction materials are selected to minimize temperature-dependent expansion.

4.3.2 Gires-Tournois Response

A Gires-Tournois interferometer replaces the second mirror with a perfect reflector. In this case $t_2=0$ and $r_2=1$. Therefore $t_{12}=0$ and the reflection coefficient (4.3.9) simplifies to

$$r_{\mathrm{GT}}=\frac{r\mathrm{e}^{-jkL}-\mathrm{e}^{jkL}}{\mathrm{e}^{-jkL}-r\mathrm{e}^{jkL}} \tag{4.3.33}$$

The magnitude is unity for all frequencies: $|r_{\mathrm{GT}}|=1$. The GT interferometer is an all-reflection filter, but the phase is frequency dependent. Making the denominator read-valued, the reflection coefficient is

$$r_{\mathrm{GT}}=\frac{\left(r\mathrm{e}^{jkL}-\mathrm{e}^{-jkL}\right)^2}{1+r^2-2r\cos(2kL)} \tag{4.3.34}$$

Denoting the phase of the reflection as $\Phi_{\mathrm{GT}}=\angle r_{\mathrm{GT}}$, the GT phase is

$$\Phi_{\mathrm{GT}}=-2\tan^{-1}\left(\frac{1+r}{1-r}\tan(kL)\right) \tag{4.3.35}$$

The phase reference plane from which Φ_{GT} is measured is located on the interface of the leading mirror.

In the limiting cases, when $r=0$ the phase propagates normally over length $2L$ while when $r=1$ the reflection is negative one. Between these two limits there is variation of the phase. The effect of the resonant cavity is more clearly shown through the group delay τ_g, where

$$\tau_g=\frac{d\Phi_{\mathrm{GT}}}{d\omega} \tag{4.3.36}$$

or, by expansion

$$\tau_g=-\frac{2n_{\mathrm{g}}L}{c}\frac{2h}{(1+h^2)+(1-h^2)\cos(2kL)} \tag{4.3.37}$$

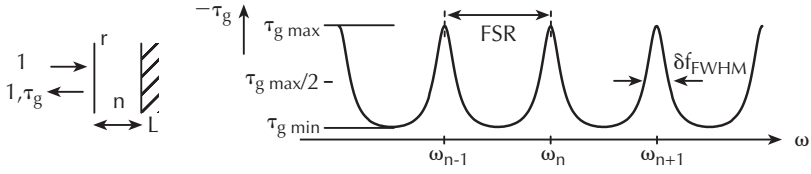

Fig. 4.6. Solid Gires-Tournois interferometer (GTI) with gap length L and refractive index n. The GTI has 100% reflection at all frequencies, but there is frequency-dependent delay of the reflection. The delay spectrum is similar to the transmission spectrum of a Fabry-Perot interferometer in that it is periodic. The FSR of the group-delay comb is dictated by the gap length and refractive index, and the maximum delay is dictated by the FSR and the reflectivity r of the partial reflector.

where

$$h = \left(\frac{1+r}{1-r}\right) \tag{4.3.38}$$

(compare (4.3.10) on page 157). Figure 4.6 illustrates an exemplar group-delay spectrum. On resonance, $2kL = 2n\pi$ and the group delay is maximum because the resonance wavelength is an integral multiple of the cavity length, allowing the storage of energy. On anti-resonance the group delay is at a minimum as there is no energy stored. Indeed the maximum and minimum group delays are

$$\tau_{g,\max} = -\frac{1}{\mathrm{FSR}}\left(\frac{1+r}{1-r}\right) \qquad 2kL = 2n\pi, \tag{4.3.39a}$$

$$\tau_{g,\min} = -\frac{1}{\mathrm{FSR}}\left(\frac{1-r}{1+r}\right) \qquad 2kL = (2n+1)\pi \tag{4.3.39b}$$

One can see that the group delay is related to the inverse of the free-spectral range and the leading mirror partial reflectivity. The inverse free-spectral range is a unit of delay for the cavity. As with the Fabry-Perot interferometer, the free-spectral range is related to cavity parameters by (4.3.20).

Conservation of Delay – Bandwidth Product

The Gires-Tournois interferometer group-delay response obeys a conservation rule in that the product of peak delay and resonance bandwidth is a constant for fixed r. Following the Fabry-Perot example, the resonance bandwidth δf_{FWHM} of the group delay can be calculated at one-half the maximum level. Setting (4.3.37) equal to $\tau_{g,\max}/2$, one finds that

$$\delta f_{\mathrm{FWHM}} = \frac{\mathrm{FSR}}{\pi\sqrt{h^2-1}} \tag{4.3.40}$$

The peak delay/bandwidth product is therefore

$$\tau_{g,\max} \times \delta f_{\mathrm{FWHM}} = -\frac{h}{\pi\sqrt{h^2-1}} = -\frac{1+r}{2\pi\sqrt{r}} \tag{4.3.41}$$

The partial reflectivity of the front mirror alone governs the peak delay/bandwidth product. The FSR of the cavity plays no role but rather is scaled out. Higher peak delays are achieved with higher reflectivities (cf. (4.3.39)), but the bandwidth (4.3.40) narrows by a commensurate amount. The partial reflectivity of the leading mirror is the only degree of freedom for this simple GT, so independent control of bandwidth and peak delay is not possible.

4.4 Temperature Dependence of Select Birefringent Crystals

There is little data available on the temperature and wavelength dependence of the refractive and group indices for components-grade birefringent crystals in the 1520–1610 nm wavelength region. Yet birefringent components such as interleavers require a detailed specification of these properties. Moreover, for components such as the off-axis compound crystals, detailed in §4.5, the design requires separate determination of the ordinary and extraordinary indices, not just their difference.

Measurement of the refractive and group indices requires different techniques. The method presented below is suitable to ascertain the temperature- and course wavelength-dependence of the group indices along the two birefringent axes. The group index accounts for first-order wavelength dependence and determines the group velocity (cf. (4.3.18)). The refractive index is defined at a specific wavelength and determines the refraction properties. The measurement technique here involves the response to a variation in the input wavelength, so it is the group index that is measured.

4.4.1 Experimental Setup

Crystal samples of YVO_4, $LiNbO_3$, α-BBO, and calcite were fabricated into Fabry-Perot resonators. The samples were cut as waveplates, with the extraordinary axis lying in the polished face of the crystal, perpendicular to the light. The sample thicknesses were nominally 1.000 mm long, and each was coated with a single thin-film layer on either face to bring the Fresnel reflectivity to approximately 50%. The parallelism specification called for less than 5 arcsec of wedge.

Figure 4.7(a) illustrates the experimental setup. The Fabry-Perot etalon response of each sample was measured with a super-luminescent diode (SLD) having 100 nm bandwidth and less than 0.25 dB ripple, and an optical spectrum analyzer with 0.05 nm resolution. The measurement band was 1515–1575 nm for all samples. The optical spectrum analyzer (OSA) was set to

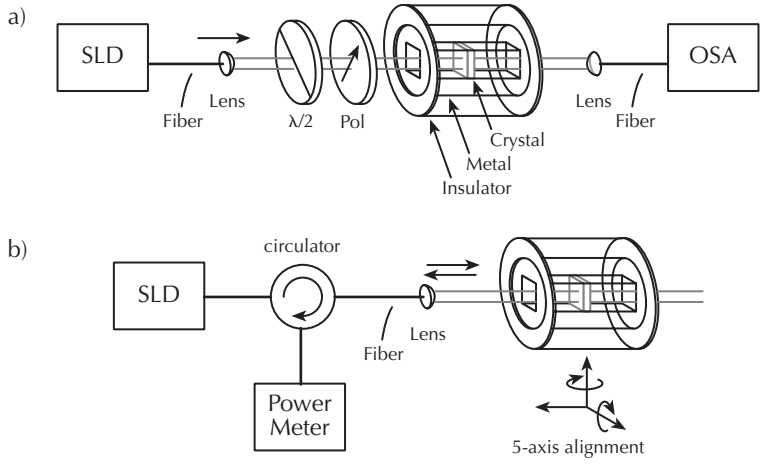

Fig. 4.7. Illustration of experimental setup to measure temperature dependence of group index. a) A superluminescent diode (SLD) provides broadband, ripple-free, polarized light in the 1515–1575 nm band. The polarizer is aligned to the extraordinary or ordinary axis of the sample crystal etalon, the latter being loaded in a heating cell. The light is collected by an optical spectrum analyzer. b) To ensure that the crystal sample is perpendicular to the light, back-reflection is collected through a circulator and the 5-axis alignment stage is adjusted to maximize this reflection.

maximum sensitivity and eight averages per scan. It is noted that the spectra were stable and averaging created little change.

To couple light through a sample, a single-mode fiber was routed from the SLD to a collimator, the collimator expanded the beam to approximately 0.75 mm in diameter, and the collimated beam transited the sample. The beam was refocused through a second lens to a single-mode fiber which was routed to the OSA. Since the samples are birefringent, an in-line Polarcor polarizer was placed before the sample. Rotation of the polarizer selected either the ordinary or extraordinary axis of the sample, or a mixture of the two. For the measurements, the polarizer was always rotated for maximum extinction of one axis or another. No measurement was made as to the extinction ratio, but visual inspection of the spectrum on the OSA indicated that the extinction was better than 10 dB. Since the SLD generates a linearly polarized white light, a half-wave waveplate was located before the polarizer and independently rotated to maximize transmission through the polarizer.

For each experiment, the sample crystal was loaded into a small brass fixture that supplied resistive heating. The aperture was rectangular and the position of one wall of the aperture was adjustable by a screw. In order to allow the crystal to expand physically the screw was lightly tightened. The brass fixture was insulated with delrin and teflon. A closed-loop temperature controller controlled the heating of the fixture to within $\pm 0.1^{\circ}$C. The samples

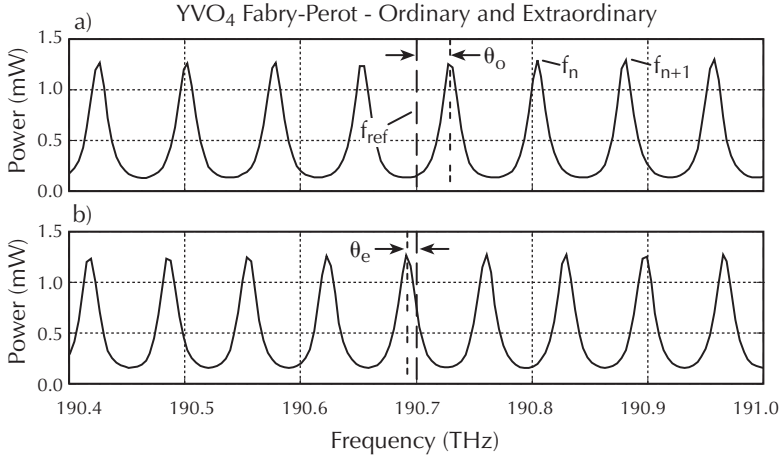

Fig. 4.8. Measured Fabry-Perot etalon response of YVO_4 crystal sample. a) Transmission response along the ordinary axis. b) Transmission response along the extraordinary axis. Note the free-spectral range along the two axes is different.

were taken from 25°C to 100°C in 5°C increments. Five minutes were allowed for thermal stabilization at each temperature.

A critical attribute of this experiment is the optical path through the sample. When the sample is canted the path length increases, but the increase is not an easily measurable quantity. To guarantee that the crystal was positioned perpendicular to the beam, a preliminary alignment was done. Figure 4.7(b) illustrates the setup with the waveplate or polarizer removed, and an optical circulator inserted between the SLD and sample. The staging that holds the sample was adjusted to maximize the back-reflection. Once maximized the sample was considered aligned. This measurement was performed before and after was temperature cycled to assess the degree of position change. It is believed that position shifts did not effect the data to within the present level of accuracy.

Figure 4.8 shows the measured transmission response of a YVO_4 etalon along the ordinary and extraordinary axes over a narrow bandwidth. In both spectra there is a comb of resonant peaks and the period of the peaks differs for the two axes. As YVO_4 is a positive uniaxial crystal, the free-spectral range of the extraordinary axis is narrower than that of the ordinary axes. Each peak, for either spectra, corresponds to a resonant mode. As the frequency is increased, more modes are added to the cavity; this is indicated at frequencies f_n and f_{n+1} in Fig. 4.8(a). Additionally, a reference frequency f_{ref} is defined to measure spectral shift with temperature. The choice of f_{ref} is arbitrary but remains constant throughout. A spectral phase θ is defined between resonant frequency f_n and the reference frequency as

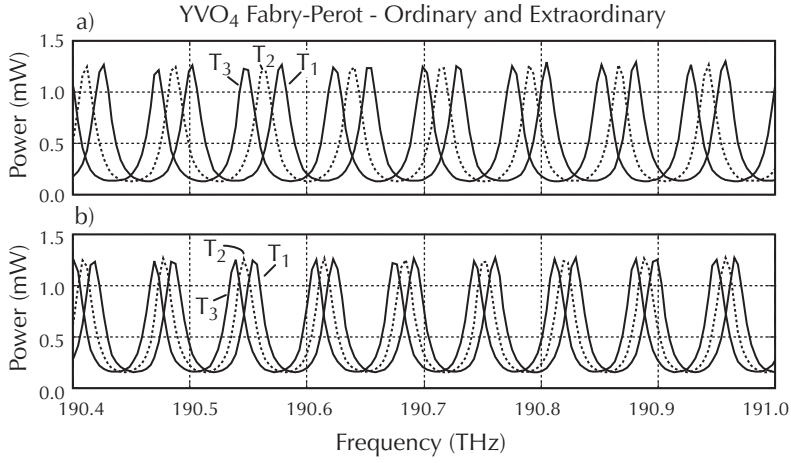

Fig. 4.9. Measured Fabry-Perot etalon response of YVO_4 crystal sample over increasing temperature, 10°C increments. The comb of resonant frequencies shifts to lower frequency, indicating an increase in the index-length product of the sample. a) Ordinary axis. b) Extraordinary axis. Note the temperature-dependent shift differs between the two axes.

$$\theta_n = 2\pi \, \frac{f_n - f_{\text{ref}}}{\text{FSR}} \tag{4.4.1}$$

This spectral phase will be used to extract the thermal-optic coefficient in the following.

Figure 4.9 shows the measured transmission response of the YVO_4 crystal as the temperature is increased from T_1 to T_3. For both axes the comb of resonant peaks shifts to lower frequencies. When the cavity expands or when the refractive index increases with increased temperature, a lower frequency is required to maintain the same mode order n that corresponds to resonant frequency f_n. The figure shows that for both the ordinary and extraordinary axes the product of the index and length increases with temperature, detuning the resonance comb to lower frequencies.

What is also evident in Fig. 4.9 is that the index-length product changes by different degrees for the ordinary and extraordinary axes. This is typical of all birefringent crystals. One effect of this birefringent temperature dependency is that the birefringent phase changes with temperature. This is a distinct disadvantage for birefringent filters that need to remain locked to the DWDM grid.

4.4.2 Quadratic Temperature-Dependence Model

The transmission expression (4.3.11) on page 157 is a function of phase $\phi = 2kL$. Expansion of the phase with temperature to second order gives

$$\phi(\Delta T) \simeq \phi_o + \phi' \Delta T + \frac{1}{2}\,\phi''(\Delta T)^2 \tag{4.4.2}$$

Similarly, the equivalent expression $2kL$ is expanded to second order as

$$\frac{2\omega}{c}\, n_{\mathrm{g}} L \simeq \frac{2\omega}{c}\left((n_{\mathrm{g}} L) + \frac{d(n_{\mathrm{g}} L)}{dT}\,\Delta T + \frac{1}{2}\,\frac{d^2(n_{\mathrm{g}} L)}{dT^2}\,(\Delta T)^2\right) \tag{4.4.3}$$

In light of these expansions, the temperature-dependent phase $\phi(\Delta T)$ can be approximated to second order as

$$\phi(\Delta T) \simeq \frac{2\pi f}{\mathrm{FSR}}\left(1 + K^{(1)}\Delta T + \frac{1}{2}\,K^{(2)}(\Delta T)^2\right) \tag{4.4.4}$$

where the linear and quadratic temperature coefficients are defined as

$$K^{(1)} = \frac{1}{n_{\mathrm{g}} L}\,\frac{d(n_{\mathrm{g}} L)}{dT} \tag{4.4.5a}$$

$$K^{(2)} = \frac{1}{n_{\mathrm{g}} L}\,\frac{d^2(n_{\mathrm{g}} L)}{dT^2} \tag{4.4.5b}$$

Extension of the temperature dependence to second order is necessary because the first-order term can be identically cancelled by proper selection of complementary crystals, as detailed in §4.4.5. However, the quadratic term cannot be so cancelled, leaving a residual error that may be significant given the requirements for telecommunications-grade components.

4.4.3 Association of Resonant Peak Shift With Temperature Coefficients

The frequency locations of the etalon resonances shift with temperature due to changes in the $n_{\mathrm{g}} L$ product. At the n^{th} resonance the optical phase is $\phi = 2n\pi$. When the temperature changes the peak frequencies shift to maintain this resonant condition. One can write the resonance frequency on the n^{th} mode for two different temperatures as

$$f_n(T_1) = \frac{nc}{2n_{\mathrm{g}} L} \tag{4.4.6a}$$

$$f_n(T_2) = \frac{nc}{2(n_{\mathrm{g}} L + \delta(n_{\mathrm{g}} L))} \tag{4.4.6b}$$

The change $\delta(n_{\mathrm{g}} L)$ can then be expressed as a function of resonant peak frequencies:

$$\frac{\delta(n_{\mathrm{g}} L)}{n_{\mathrm{g}} L} = \frac{f_n(T_1)}{f_n(T_2)} - 1 \tag{4.4.7}$$

Using the quadratic expansion (4.4.3) and temperature coefficient definitions (4.4.5), the ratio of resonant frequencies is related to the temperature dependence as

$$\frac{f_n(T)}{f_n(T+\Delta T)} - 1 = K^{(1)}\Delta T + \frac{1}{2}\,K^{(2)}(\Delta T)^2 \tag{4.4.8}$$

If the frequency peaks can unambiguously be determined from the data, then estimates of $K^{(1)}$ and $K^{(2)}$ can be determined from (4.4.8).

A problem with the determination of $f_n(T)$ is that the resonant peak locations of the etalon do not coincide with the frequencies at which the OSA measures the transmitted power. This can be observed by close inspection of Fig. 4.8. The periodic nature of the spectrum, however, can be used to advantage by applying a Fourier analysis. Using a Fourier transform to extract the spectral phase of a mode provides a certainty enhancement of the phase value. The phase difference between two temperatures determines $f_n(T+\Delta T)$ via

$$f_n(T+\Delta T) = \frac{\mathrm{FSR}}{2\pi}\,(\theta_n(T+\Delta T) - \theta_n(T)) + f_n(T) \tag{4.4.9}$$

as long as $\mathrm{FSR}(T+\Delta T) \simeq \mathrm{FSR}(T)$.

There is a certain tradeoff for the Fourier analysis. On one hand the spectral phase accuracy is improved by taking the Fourier transform over a large number of periods. On the other hand, association of the resultant spectral phase to a particular mode is increasingly less certain as the transform window includes more modes. The presence of $f_n(T)$ on the right-hand side of (4.4.9) requires a certainty of the mode to which the spectral phase is associated. The wavelength range for these measurements is 1515–1575 nm, or about 3.9% spectral coverage. If the Fourier transform were taken over, the entire data set there would be a $\pm 2\%$ error is certainty of f_n.

The tradeoff used here is to partition the data set into subsets having 128 points, or about 3.8 nm, each. The certainty of f_n is then $\pm 0.12\%$. The spectral phase of the fundamental tone for each partition was extracted from its Fourier transform, and the sequence of phases for a temperature ramp was inserted into (4.4.9). This was done for each data partition and the results were compared. Overall, there was no discernible trend from partition to partition, although small differences were evident.

For each partition and at each temperature the free-spectral range was estimated via

$$\mathrm{FSR}^{(\mathrm{est})}(T) = \frac{f_k(T) - f_j(T)}{N_p - 1} \tag{4.4.10}$$

where the approximate peak frequencies $f_{j,k}$, were taken at either end of the partition, and N_p is the number of peaks in a partition. The FSR estimates over all temperatures were compared. There was no trend of the FSR estimates, which is reasonable since only one or two modes were added over the total temperature range, depending on the material.

4.4.4 Group Index and Thermal-Optic Coefficients

Table 4.6 tabulates the results of the data analysis, and Figs. 4.10-4.11 show the determination of $\delta(n_{\mathrm{g}}L)$ over temperature for the four crystals. The co-

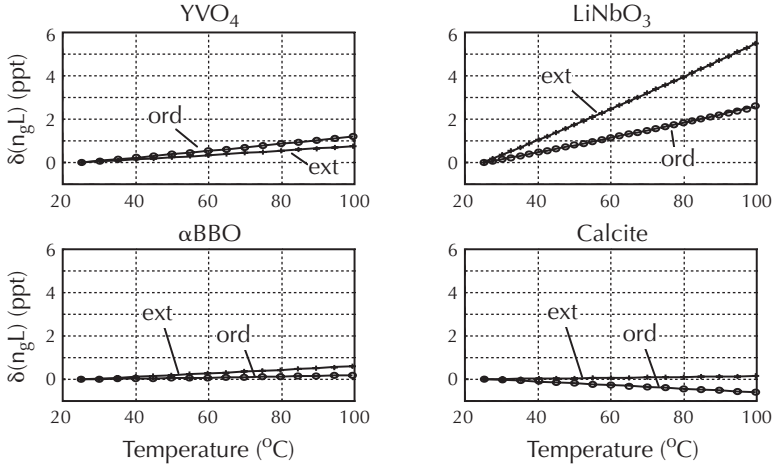

Fig. 4.10. Measured and quadratically fit temperature-dependent refractive index change for select crystals. The ordinary and extraordinary axes are separately measured. $LiNbO_3$ has a much larger thermal-optic effect than the other crystals. Calcite has a negative thermal-optic effect on the ordinary axis.

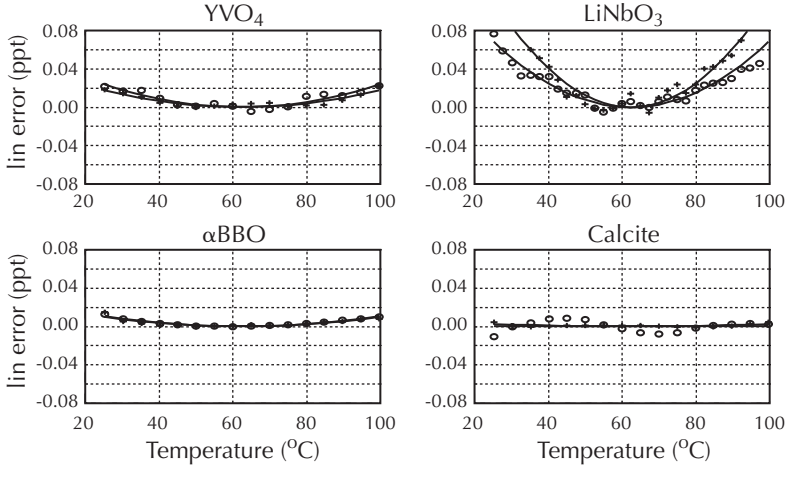

Fig. 4.11. Measured and estimated quadratic residual change in index, with the linear term removed. $LiNbO_3$ has a large quadratic shift. Calcite shows a spurious undulation along the ordinary axis.

Table 4.6. Group Index and Thermal-Optic Coefficients

Property	YVO_4	$LiNbO_3$	α-BBO	Calcite	**Units**
$n_{g,e}$	2.1918	2.1834	1.5296	1.4832	
$n_{g,o}$	1.9770	2.2656	1.6593	1.6593	
Δn_g	+0.2148	−0.0822	−0.1297	−0.1761	
$K_e^{(1)}$	4.9077	32.228	5.2729	1.3008	$\times 10^{-6}$/K
$K_o^{(1)}$	8.1226	15.351	1.7364	−4.9372	$\times 10^{-6}$/K
$K_{\Delta n}^{(1)}$	−24.682	−432.93	−39.971	−57.477	$\times 10^{-6}$/K
$K_e^{(2)}$	0.0112	0.0707	0.0069	0.0035	$\times 10^{-6}$/K
$K_o^{(2)}$	0.0149	0.0424	0.0061	−0.0009	$\times 10^{-6}$/K
$K_{\Delta n}^{(2)}$	−0.0224	−0.7093	−0.0033	−0.0380	$\times 10^{-6}$/K

Measurement range: 1515–1575 nm, 25°C–100°C.

$\Delta T = 0$ at $T = 62.5$°C.

efficients were generated for $\Delta T = 0$ at $T_o = 62.5$°C. Figure 4.10 shows the change of the group-index–length product as a function of temperature, the room-temperature group index being subtracted from the data to better show the variation. The solid lines are the quadratic curve fit. $LiNbO_3$ is clearly the most temperature-dependent material of the four. Calcite has a negative thermal-optic coefficient for its ordinary axis. Whether the negative coefficient comes from change in group index or length cannot be distinguished from this experiment.

Figures 4.11 shows the same data as in Fig. 4.10 but with the best-fit linear slope removed. This highlights the deviation from linear temperature dependence. Again, $LiNbO_3$ has the largest quadratic effect. Calcite shows an irregular undulation for the ordinary axis. The quadratic terms for YVO_4 and α-BBO are small but may be significant.

In some cases the thermal-optic coefficient K for the birefringence needs to be known, rather than the coefficient for either index. The birefringent coefficient for linear and quadratic terms is derived from

$$K_{\Delta n_g}^{(1,2)} = \frac{1}{\Delta n_g}\left(n_{g,e}K_e^{(1,2)} - n_{g,o}K_o^{(1,2)}\right) \tag{4.4.11}$$

Passive compensation of birefringent phase requires this combined coefficient.

4.4.5 Passive Temperature Compensation

In applications of birefringent filters, birefringent crystals cut as waveplates are used to generate a periodic filter response. The periodicity is generated by

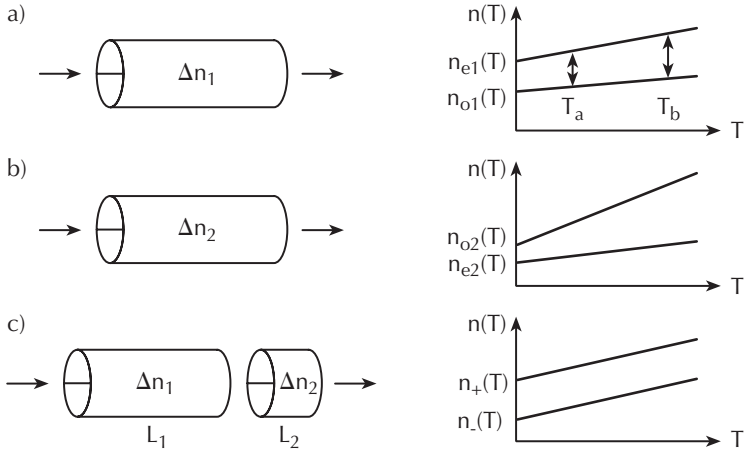

Fig. 4.12. Passive temperature compensation of birefringent phase. a) A birefringent crystal cut as a waveplate, line in face indicates extraordinary axis. Temperature dependence of refractive index for ordinary and extraordinary indices differs, as indicated on the right graph. b) Another birefringent crystal having different thermal-optic coefficients from a). c) Length ratio of two crystals is designed so that temperature dependencies of n_+ and n_- are matched. The birefringent phase of the cascade is temperature-compensated to first order.

the frequency-dependent polarization transformation of the waveplate rather than by the Fabry-Perot effect discussed in the preceding sections. Like the Fabry-Perot interferometers, the comb spectrum of a waveplate shifts in frequency due to the temperature dependence of the birefringence.

The birefringent phase φ is defined through the difference between extraordinary and ordinary indices as

$$\varphi = \frac{\omega}{c}\,(n_e - n_o)\,L \tag{4.4.12}$$

A change in temperature changes the phase, to first order, as

$$\Delta\varphi = \frac{\omega}{c}\,(n_e K_e - n_o K_o)\,L(\Delta T) \tag{4.4.13}$$

Consider for example a YVO_4 waveplate that is 10 mm long, and the temperature is changed by 75°C. Using the entries from Table 4.6 one finds the birefringent phase changes by $\Delta\varphi \simeq -2.6\lambda$, or over two waves. The comb spectrum shifts by more than two beats. For a $LiNbO_3$ waveplate of equal length the birefringent phase shifts $\Delta\varphi \simeq 17.1\lambda$.

Figure 4.12(a,b) illustrates this reason for the change. The ordinary and extraordinary indices generally have different thermal-optic coefficients, which in turn causes a temperature-dependent shift in birefringent phase.

To correct for first-order temperature dependence, two complementary crystals can be cascaded. As illustrated in Fig. 4.12(c), given the correct length

ratio the temperature dependence on one polarization axis can be adjusted to equal the temperature dependence on the orthogonal polarization axis. The term "polarization axis" is used here because the extraordinary axes of the two crystals may be aligned or crossed, depending on the materials, so the designation of extraordinary axes for the combination loses its meaning.

In practice, an athermal crystal pair is designed for a specific free-spectral range. The length ratio of the pair sets the athermalization and the length total sets the free-spectral range. The free-spectral range for a waveplate is determined from the differential group delay τ, where τ is defined as

$$\tau = \frac{\partial \varphi}{\partial \omega} = \frac{\Delta n_{\mathrm{g}} L}{c} \tag{4.4.14}$$

and the waveplate free-spectral range is $\mathrm{FSR} = 1/\tau$. Note that the FSR of a waveplate is different from a Fabry-Perot (4.3.20): the waveplate FSR is governed by its group-index difference and crystal length (see (3.6.35) on page 121); the Fabry-Perot FSR is governed by the group index and twice the cavity length. The combination of two crystals gives a total differential group delay of

$$\tau_s = \tau_1 + \tau_2 \tag{4.4.15a}$$

$$= \left(\Delta n_{\mathrm{g},1} L_1 \pm \Delta n_{\mathrm{g},2} L_2\right)/c \tag{4.4.15b}$$

where the + and − signs refer to parallel and perpendicular alignment, respectively, of the extraordinary axes of the two crystals.

The temperature dependence of the birefringent phase to first order is

$$\frac{\partial \varphi}{\partial T} = \frac{\omega}{c}\, \Delta n_{\mathrm{g}} L K^{(1)}_{\Delta n_{\mathrm{g}}} \tag{4.4.16}$$

Stripping unnecessary sub- and superscripts, the combined temperature dependence is cancelled when

$$\frac{\omega}{c}\ \left(\Delta n_1 L_1 K_1 \pm \Delta n_2 L_2 K_2\right) = 0 \tag{4.4.17}$$

where the ± sign has the same meaning as for (4.4.15b). Combining (4.4.15b) and (4.4.17), the length ratio is

$$L_2/L_1 = \mp \frac{\Delta n_1 K_1}{\Delta n_2 K_2} \tag{4.4.18}$$

and the length of the first crystal is

$$L_1 = \frac{c\tau_s}{\Delta n_1 \pm \Delta n_2 (L_2/L_1)} \tag{4.4.19}$$

The one necessary variable to attain a solution for any pair of crystals is the alignment or crossing of the extraordinary axes. Table 4.6 shows that

Table 4.7. Passive Temperature Compensation Combinations

Combination	L_1 (mm)	L_2 (mm)	$L_1 + L_2$ (mm)
YVO_4 ∥ $LiNbO_3$	14.801	2.205	17.005
YVO_4 ∥ α-BBO	36.488	37.315	73.803
YVO_4 ∥ Calcite	24.461	12.812	37.273
α-BBO ⊥ $LiNbO_3$	25.465	3.710	29.175
Calcite ⊥ $LiNbO_3$	19.630	5.583	25.213
α-BBO ⊥ Calcite	75.890	38.870	114.761

$L_1 + L_2$ generates $\tau_s = \pm 10.0$ ps.

∥ and ⊥ indicate aligned or crossed extraordinary axes, respectively.

the signs for the birefringent thermal-optic coefficients are the same for all crystals. However, YVO_4 is positive uniaxial and the rest are negative uniaxial. Referring to (4.4.17), if the birefringence of a crystal pair has the same sign the extraordinary axes must be crossed; otherwise they are aligned.

Table 4.7 tabulates the crystal lengths required for all six combinations of crystal pairs such that the pair generates $\tau_s = \pm 10$ ps. Clearly the YVO_4 and $LiNbO_3$ combination yields the shortest total length.

The residual phase error is calculated from the quadratic deviation. Similar to 4.4.13, the quadratic error is

$$\Delta\varphi = \frac{\omega}{2c}\left(\Delta n_1 L_1 K_1^{(2)} \pm \Delta n_2 L_2 K_2^{(2)}\right)(\Delta T)^2 \tag{4.4.20}$$

For the YVO_4-$LiNbO_3$ combination at $f = 194.1$ THz and $\Delta T = 37.5°C$, $\Delta\varphi \simeq 0.026\lambda$. This is a several order-of-magnitude decrease in temperature dependence of birefringent phase as compared with either crystal separately.

4.5 Compound Crystals For Off-Axis Delay

Applications such as birefringent filters and polarization-mode dispersion (PMD) sources require the cascade of several crystals of equal length or having integral multiples of a unit length. The Lyot filter as adopted to interleavers is a classic example. But birefringent crystals are expensive and if the light beam is to pass through a cascade of equal-length crystals it would be better to fold the beam to pass through the same crystal several times. This has been proposed for both interleavers [13] and PMD generators [15]. For either component, after each pass of the crystal the polarization is rotated with a waveplate; the delay (crystal)/rotation (waveplate) sequence can be designed to make a birefringent filter.

There remains a problem, however. The problem is the beam must enter and exit the crystal, or temperature-compensated crystal pair, normal to the input face or else suffer double refraction. Double refraction is compounded by every pass and results in polarization-dependent loss. This is illustrated in Fig. 4.13(a). Here an off-normal beam is double-refracted by a first high-birefringent crystal. The two beams inside the crystal walkoff from one another and emerge offset. After polarization rotation from the intermediate waveplate, the two beams enter the second crystal and are each double refracted. Four beams emerge from the second crystal: however, the center two will overlap if the two crystal lengths are identical. Since the displaced beams will couple to a receiving collimator with different efficiencies, the concatenation generates PDL.

Double refraction for off-normal incidence onto a waveplate-cut crystal must be accepted because one polarization will see an effective index; the other, the ordinary index. This effect is treated in §3.6.2. One solution that fixes the walkoff problem but does not otherwise work is illustrated in Fig. 4.13(b). Here two equal-length crystals of the same material are placed with e-axes perpendicular to one another. The crystals are either both positive or negative uniaxial. The double refraction of the first crystal is corrected by the second crystal because extraordinary and ordinary rays are exchanged with one another. However, as shown in Fig. 4.13(c), the exchange used to cancel the net walkoff also exchanges the fast and slow axes; the delay imparted by the first crystal is cancelled by an equal and opposite delay from the second. In principle there is no net effect.

Inspection of Fig. 3.13 on page 114 shows that there is a solution for a birefringent delay having zero net walkoff with off-normal incidence. Any solution focuses on the Poynting vector directions, not the k-vector directions. One possible configuration is shown in Fig. 4.14(a): a positive uniaxial crystal is followed by a negative uniaxial crystal oriented such that the extraordinary axes are perpendicular [16]. In the first crystal the e-ray is refracted more than the ordinary ray because the crystal is positive uniaxial, Fig. 4.14(b). However, the e-Poynting vector is deflected by the refraction less than the ordinary Poynting vector. That is, the o-Poynting vector lies between the extraordinary Poynting and k-vectors. The e-Poynting vector splits from its k-vector because its linear polarization state is neither parallel nor perpendicular to the e-axis of the first crystal.

Entrance into the second crystal exchanges the designations of two rays. Also, both polarization states are either parallel or perpendicular to the e-axis, so there is no further splitting of the e-Poynting vector. Even though the o- and e-ray designations are flipped, the slow ray remains slow and the fast ray remains fast because the second crystal is negative uniaxial. Moreover, examination of the Poynting vectors shows that they will converge in the second crystal. The length ratio of the first and second crystal can be designed to impart a target delay and yield zero net walkoff.

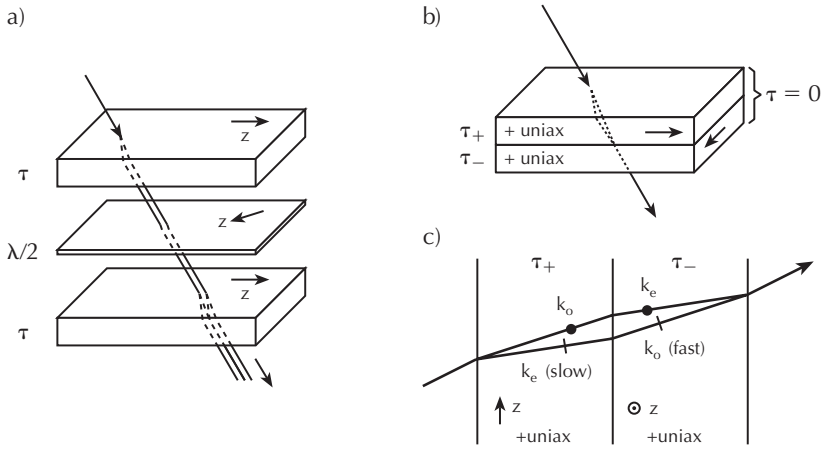

Fig. 4.13. Off-axis incidence angle. a) Off-axis passage through two delay crystals with an intermediate waveplate that rotates polarization (as in a filter) creates beam-splitting due to double refraction. The multiple output beams produce PDL. b) A "solution" that has zero net walkoff but no accrued delay. Two like crystals are placed perpendicular to one another. c) Ray trace of k-vectors. Fast exchanges with slow. No net delay.

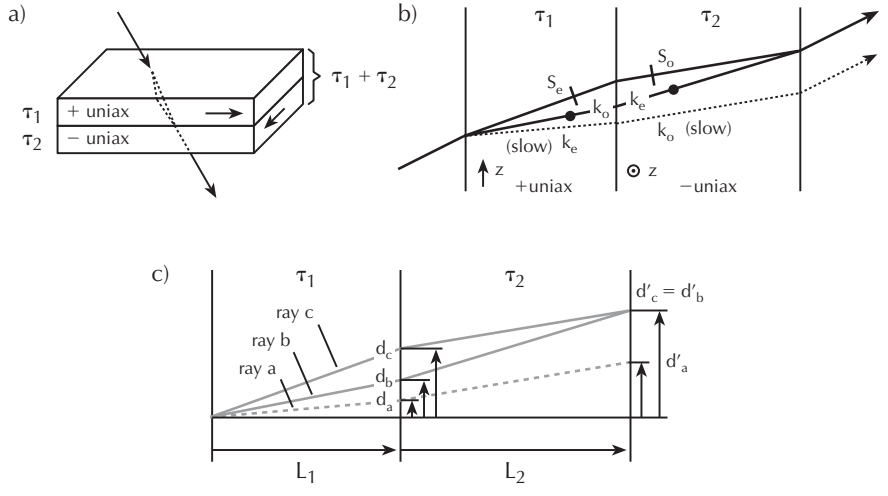

Fig. 4.14. An off-axis zero net walkoff crystal pair that accrues delay. a) Two different crystals with e-axes perpendicular, the first crystal is positive uniaxial and the second negative uniaxial. b) Ray trace. The e-Poynting vector splits from its k-vector in the first crystal, undergoing less deflection than the o-Poynting vector but at slower speed. In second crystal $e \leftrightarrow o$ but the slow path remains slow. c) Proper length ratio L_2/L_1 achieves zero net walkoff.

The length ratio for a two-crystal solution is calculated by equating the cumulative displacement of the two Poynting vectors. Figure 4.14(c) illustrates an a-ray, a b-ray, and a c-ray. The a-ray is the k-vector of the e-ray in the first crystal, the b-ray is the k- and Poynting vectors for the o-ray, and the c-ray is the Poynting vector of the e-ray. The b- and c-rays are to converge.

For small inclination angles all refraction expressions are linearized to good approximation. The displacements through the first crystal are

$$\begin{aligned} d_b(L_1) &= \theta_b^{(1)} L_1 \\ d_c(L_1) &= \left(\theta_a^{(1)} + \gamma\right) L_1 \end{aligned}$$

where $\theta_a^{(1)}$ and $\theta_b^{(1)}$ are the refraction angles and γ is the Poynting-vector tilt angle within the first crystal. The cumulative displacements through the second crystal are

$$\begin{aligned} d_b(L_1 + L_2) &= d_b(L_1) + \theta_b^{(2)} L_2 \\ d_c(L_1 + L_2) &= d_c(L_1) + \theta_a^{(2)} L_2 \end{aligned}$$

where $\theta_a^{(2)}$ and $\theta_b^{(2)}$ are the refraction angles in the second crystal. Zero net walkoff is achieved for $d_b(L_1 + L_2) = d_c(L_1 + L_2)$. This condition gives

$$\frac{L_2}{L_1} = \frac{\gamma - \left(\theta_b^{(1)} - \theta_a^{(1)}\right)}{\theta_b^{(2)} - \theta_a^{(2)}} \tag{4.5.1}$$

Taking the ambient index as one, the linearized refraction angles are

$$\theta_a^{(1)} = \theta_o / n_{e,1}, \quad \theta_b^{(1)} = \theta_o / n_{o,1}, \quad \theta_a^{(2)} = \theta_o / n_{e,2}, \quad \text{and} \quad \theta_b^{(2)} = \theta_o / n_{o,2}$$

The Poynting-vector tilt angle γ, that is, the angle at which the vector tilts away from its corresponding k-vector, comes from linearization of (3.6.15) on page 110 where $\theta \simeq 90°$. As the negative tilt has already been accounted for, the linearized tilt angle is

$$\gamma = \frac{\left(n_{e,1}/n_{o,1}\right)^2 - 1}{n_{e,1}}\, \theta_o$$

In terms of refractive indices, the length ratio is

$$\frac{L_2}{L_1} = \frac{n_{o,2}}{n_{o,1}} \frac{(n_{e,1}/n_{o,1} - 1)}{(n_{o,2}/n_{e,2} - 1)} \tag{4.5.2}$$

This ratio is positive when the first crystal is positive uniaxial and the second crystal is negative uniaxial. A YVO_4 and α-BBO crystal will satisfy this equation. One can verify that for this length ratio, the change in net displacement

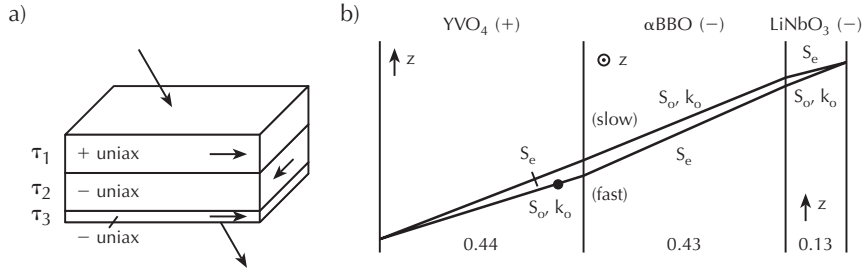

Fig. 4.15. Three crystal solution: accrued delay with zero net walkoff with inclined incidence and first-order temperature compensation. a) Specific crystal design. b) Ray trace of Poynting vectors. The Poynting vector is split from the e-ray k-vector in the first and third crystal.

for a change of incident angle is zero to first order. That is, net walkoff grows as second order with change in incident angle, making the compound crystal more tolerant to alignment.

An effective index for the crystal pair can be defined as $n_{\text{eff}} = \theta_o/\theta_{\text{eff}}$. The effective refraction angle is the ratio of total displacement to length, or $d_c = \theta_{\text{eff}}\,(L_1 + L_2)$. Combining terms gives

$$n_{\text{eff}} = \frac{L_2/L_1 + 1}{L_2/L_1 + n_{o,2}/n_{o,1}}\, n_{o,2} \tag{4.5.3}$$

The remaining problem is that the two crystals necessary to make the compound crystal are not necessarily temperature compensated. The one degree of freedom available, the length ratio, was used to enforce zero net walkoff. To make the compound crystal temperature insensitive as well a third crystal is necessary (Fig. 4.15(a)). Here YVO_4, α-BBO, and $LiNbO_3$ crystals stacked so that the e-axis of the α-BBO crystal is perpendicular to the other two axes give a solution.

A set of three linear equations can be solved to determine the three crystal lengths such that there is zero net walkoff, temperature is compensated to first order, and a target delay τ is achieved. In matrix form the equations are

$$\begin{pmatrix} \alpha_1 & -\alpha_2 & \alpha_3 \\ \Delta n_1 K_1 & -\Delta n_2 K_2 & \Delta n_3 K_3 \\ \Delta n_1 & -\Delta n_2 & \Delta n_3 \end{pmatrix} \begin{pmatrix} L_1 \\ L_2 \\ L_3 \end{pmatrix} = \begin{pmatrix} 0 \\ 0 \\ \tau c \end{pmatrix} \tag{4.5.4}$$

where K is the first-order temperature coefficient defined by (4.4.5a) (but for the refractive index, not group index), and the angle differences α are

$$\alpha_1 = \gamma - \left(\theta_b^{(1)} - \theta_a^{(1)}\right) = \frac{n_{e,1}}{n_{o,1}} \left(\frac{1}{n_{o,1}} - \frac{1}{n_{e,1}}\right) \theta_o \tag{4.5.5a}$$

$$\alpha_2 = \theta_b^{(2)} - \theta_b^{(1)} = \left(\frac{1}{n_{e,2}} - \frac{1}{n_{o,2}}\right) \theta_o \tag{4.5.5b}$$

$$\alpha_3 = \gamma - \left(\theta_b^{(3)} - \theta_a^{(3)}\right) = \frac{n_{e,3}}{n_{o,3}} \left(\frac{1}{n_{o,3}} - \frac{1}{n_{e,3}}\right) \theta_o \tag{4.5.5c}$$

The negative sign in the second column of (4.5.4) accounts for the perpendicular orientation of the α-BBO e-axis with respect to the other crystals.

Group index and thermal coefficients for YVO_4, α-BBO, and $LiNbO_3$ are found in Table 4.6. The refractive indices were not measured for this table, but it was observed that the frequency dependence of the index was below an observable level. So the refractive indices are approximated by the group indices. Using the tabulated values, a YVO_4 crystal of length $L_{\rm yvo} = 9.49$ mm, an α-BBO length of $L_{\rm abbo} = 9.37$ mm, and a $LiNbO_3$ length of $L_{\rm ln} = 2.84$ mm satisfies (4.5.4). The ray-trace of the Poynting vectors is shown in Fig. 4.15(b).

The practical drawback of temperature-compensated birefringent crystal sets, either on-axis or off-axis, is the widely disparate, highly anisotropic thermal expansion coefficients. This is seen in Tables 4.2 and 4.3. Coupling these materials with glasses and packaging alloys makes for a complex thermal design which stretches the ability to achieve athermal birefringent phase over a 70° operating range or more. The on-axis athermal crystal set of YVO_4 and $LiNbO_3$ has been used quite successfully, however, in the laboratory environment.

4.6 Polarization Retarders

Polarization retarders are essential parts used to build birefringent components such as isolators, circulators, interleavers, and polarization mode dispersion generators. Broadly speaking, a retarder is any optical element that transforms the state of polarization without loss. Birefringent crystals cut as waveplates, electro-optic materials, optically active materials, Faraday media, and total-internal reflection rhombs can all transform polarization. The distinguishing attribute is that two polarization components slip in phase within the medium, transforming its polarization state.

As a comment on nomenclature, retardation and birefringent phase represent the same physical effect. Both characterize a phase slip between two co-propagating waves having different wavelengths. The nuance is that retardation denotes the fractional phase slip when the overall slip is zero, one, or a few birefringent beats. As used in this text, birefringent phase is the total phase slip, fractional and integral, between two co-propagating plane waves of dissimilar wavelength.

The preponderance of this section analyzes birefringent waveplate retarders and select combinations. Highly multi-order waveplates and the thermal stabilization of birefringent phase were covered in §4.4. Total internal reflection retarders are covered last.

4.6.1 Half-Wave and Quarter-Wave Waveplates

The calculus of polarization transformation is extensively treated in Chapter 2 and the reader is particularly directed to §2.6. These tools are used below to write by inspection the transformation matrix operators and vector expressions for quarter- and half-wave waveplates.

A waveplate is made of birefringent material such as solid crystals, polyimide films, or liquid crystals, to cite a few. The waveplate technologies addressed in this section are solid crystals, for the formalism for polarization transformation is applicable to any technology. A waveplate made from birefringent crystal, typically a uniaxial crystal, is cut so that the extraordinary axis lies in the crystal face. Drawing from §3.6.4, the birefringent phase of a waveplate is defined by

$$\varphi = \frac{\omega}{c}\,(n_e - n_o)\,L \tag{4.6.1}$$

where L is the length of the crystal. Half- and quarter-wave waveplates generate the birefringent phases

$$\varphi_{\lambda/2} = (2n+1)\pi \tag{4.6.2a}$$

$$\varphi_{\lambda/4} = \left(2n + \frac{1}{2}\right)\pi \tag{4.6.2b}$$

respectively, where the order n is a positive integer including zero. The length of an arbitrary order half-wave waveplate is

$$L_{\lambda/2} = \left(\frac{2n+1}{2}\right)\frac{\lambda}{\Delta n} \tag{4.6.3}$$

where $\lambda/\Delta n$ is recognized as the birefringent beat length in the crystal. Clearly, as the order decreases so does the plate length. A true zero-order ($n = 0$) half-wave plate fabricated from crystalline quartz for $\lambda = 1545$ nm is about 92 μm thick, which requires special care to fabricate. The extra cost associated with the true zero-order plate is why low-order waveplates are attractive for many non-telecommunications applications. The polarization transformation of a waveplate of any retardation φ is given in Jones space by (2.6.19) on page 68 and in Stokes space by (2.6.25) on page 68, where the birefringent axis post-fix operators are resolved into matrix form via (2.6.29) on page 70.

Consider a waveplate with extraordinary axis rotated by θ to the horizontal in the plane perpendicular to propagation direction. The birefringent vector $\hat{r}$ in Stokes space is

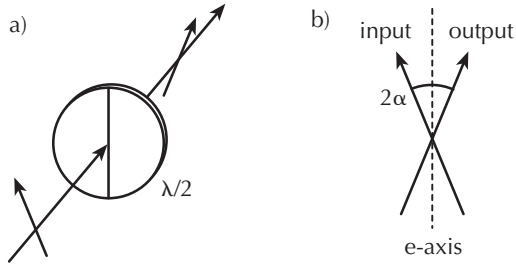

Fig. 4.16. Mirror image produced by a perfect half-wave waveplate. a) Incident linear polarization vector is mirror imaged about the extraordinary axis, producing a vector with the opposite tilt. b) Mirror image of a linear input state inclined to the extraordinary axis by α appears as a rotation by 2α.

$$\hat{r}(\theta) = \begin{pmatrix} \cos 2\theta \\ \sin 2\theta \\ 0 \end{pmatrix} \tag{4.6.4}$$

For a half-wave waveplate, the retardation is $\varphi = \pi$ and the Jones matrix operator is

$$U_{\lambda/2}(\theta) = -j \begin{pmatrix} \cos 2\theta & \sin 2\theta \\ \sin 2\theta & -\cos 2\theta \end{pmatrix} \tag{4.6.5}$$

The -1 coefficient to the second diagonal term indicates a mirror image. The equivalent Stokes operator in vector form is

$$R_{\lambda/2} = 2(\hat{r}\hat{r}\cdot) - I \tag{4.6.6}$$

When resolved onto the basis implicit in (4.6.4), the Stokes matrix operator is

$$R_{\lambda/2}(\theta) = \begin{pmatrix} \cos 4\theta & \sin 4\theta & 0 \\ \sin 4\theta & -\cos 4\theta & 0 \\ 0 & 0 & -1 \end{pmatrix} \tag{4.6.7}$$

Again the mirror image is apparent. A perfect half-wave waveplate generates the mirror image

$$(S_1, S_2, S_3) \longrightarrow (S_1, -S_2, -S_3) \tag{4.6.8}$$

along with rotation by 4θ about S_3. The Stokes matrix operator imparts a fourfold multiple of the physical waveplate angle θ in its arguments. This is accounted for by first considering the $2\times$ multiple that results by going from Jones to Stokes space, and then the $2\times$ multiple generated by the mirror-image of the input state about the birefringent axis. Figure 4.16 illustrates the mirror image effect of a perfect half-wave waveplate and its apparent rotation about the birefringent axis. Figure 4.17(a) illustrates the Stokes space view of an $n = 0$ half-wave waveplate transformation. Polarization state a rotates to state b by precession about $\hat{r}$ by $\varphi = \pi$. Note that when the input state is linear (lies on the equator) the output is its orthogonal state.

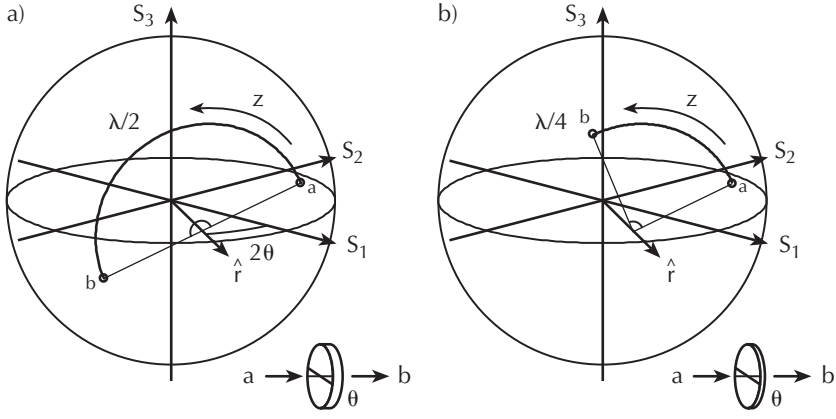

Fig. 4.17. Half-wave and quarter-wave waveplate transformations in Stokes spaces. a) Stokes picture of half-wave transformation. Birefringent axis $\hat{r}$ lies on the equator and is rotated by 2θ from S_1. The birefringent axis corresponds to the extraordinary axis of the crystal. Input state a is transformed to b by $\varphi = pi$ about $\hat{r}$. b) Stokes picture of quarter-wave transformation. Input state a rotates to b through $\varphi = \pi/2$.

For a quarter-wave waveplate rotated by θ, the retardation is $\varphi = \pi/2$ and the Jones matrix operator is

$$U_{\lambda/4}(\theta) = \frac{1}{\sqrt{2}} \begin{pmatrix} 1 - j\cos 2\theta & -j\sin 2\theta \\ -j\sin 2\theta & 1 + j\cos 2\theta \end{pmatrix} \tag{4.6.9}$$

The equivalent Stokes operator in vector form is

$$R_{\lambda/4} = (\hat{r}\hat{r}\cdot) + (\hat{r}\times) \tag{4.6.10}$$

When resolved onto the basis implicit in (4.6.4), the Stokes matrix operator is

$$R_{\lambda/4}(\theta) = \begin{pmatrix} \cos^2 2\theta & \sin 2\theta \cos 2\theta & \sin 2\theta \\ \sin 2\theta \cos 2\theta & \sin^2 2\theta & \cos 2\theta \\ -\sin 2\theta & \cos 2\theta & 0 \end{pmatrix} \tag{4.6.11}$$

Since no mirror image is derived from the quarter-wave plate, the arguments in $R_{\lambda/4}$ retain their $2\times$ multiple. The Stokes operator matrix is more complex as a result. Figure 4.17(b) illustrates the Stokes space view of an $n = 0$ quarter-wave waveplate transformation. Polarization state a rotates to state b via precession about $\hat{r}$ by $\varphi = \pi/2$.

Frequency Dependence

Birefringent phase (4.6.1) is directly proportional to optical frequency ω. The chromatic dependence is

$$\frac{d\varphi}{d\omega} = \varphi\left(\frac{1}{\omega} + \frac{1}{\Delta n_{\mathrm{g}}}\frac{d(\Delta n_{\mathrm{g}})}{d\omega}\right) \tag{4.6.12}$$

Even excluding material dispersion, the chromatic dependence depends directly on the target value of φ:

$$\Delta\varphi = \frac{\Delta\omega}{\omega}\,\varphi \tag{4.6.13}$$

Waveplate order plays a role in the chromatic dependence. There is a direct tradeoff between the ease of fabrication versus the birefringent phase variation. For example, the frequency-dependent birefringent phase change for an n^{th}-order half-wave waveplate is

$$\Delta\varphi_{\lambda/2} = \frac{\Delta\omega}{\omega}\,(2n+1)\,\pi \tag{4.6.14}$$

The change is a function of the retardation and the spectral bandwidth. Consider the spectral coverage for the C-band (4.1.5): $\mathcal{S}_C \simeq 2\%$. The change of birefringent phase across this band for three different waveplate orders is

$$\Delta\varphi_{\lambda/2} = \begin{cases} \pm 1.8^\circ & n = 0, \\ \pm 5.4^\circ & n = 1, \\ \pm 37.8^\circ & n = 10 \end{cases} \tag{4.6.15}$$

The change increment from zero order to first order alone imparts a threefold increase in chromatic dependence. Conversely, the bandwidth for a fixed $\Delta\varphi$ tolerance suffers a threefold decrease.

Depending on design requirements, waveplates in a component may have to be eliminated where possible to broaden the spectrum over which the component specifications are held. For example, in a circulator the extraordinary axes of the birefringent prisms can be cut in non-standard ways to align to the polarization axes rather than have a waveplate make the rotation. For other components where a waveplate is absolutely required, achromats made from waveplate combinations can in some cases be used.

4.6.2 Birefringent Waveplate Technologies

Fabrication of a waveplate requires high accuracy between the target retardation and the actual retardation of the part. Low-order waveplates are single- or double-side polished and the retardation is directly measured by interrupting the process. The waveplate is compared to a reference standard at the target wavelength and polishing continues until the waveplate is within tolerance.

So that there is minimum retardation change for each polish step, a very low birefringent material is used, such as crystalline quartz. Quartz has a birefringence of $\Delta n = 0.0084$ at 1.55 μm and associated birefringent beat length of $\Lambda \sim 184$ μm. A typical quartz waveplate is specified to within $\lambda/500$, which

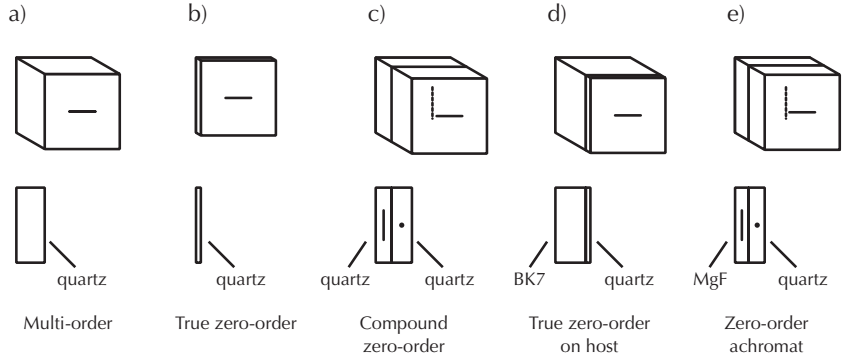

Fig. 4.18. Illustrations of solid-crystal waveplate technologies. a) Multi-order waveplate, single block of, e.g., quartz. b) True zero-order waveplate. Minimum thickness given the material birefringence to achieve required retardance. c) Compound zero-order waveplate makes for easier fabrication but poorer extinction ratio and angular aperture. d) Optically contacted true zero-order waveplate, very useful because quarter-wave waveplates of quartz, a low-birefringent material, are 45 μm thick at zero order. e) Zero-order achromat, such as MgF_2/crystalline quartz.

corresponds to a ± 0.2 μm tolerance. Only with optical feedback is this tolerance possible.

Figure 4.18 illustrates five common types of waveplates. The easiest part to make is a multi-order waveplate (Fig. 4.18(a)). This waveplate has a thickness of $t = m\lambda/\Delta n + \delta t$, where m is the waveplate order, Δn is the birefringence, and δt is the minimum thickness required to achieve the target retardation. A half-wave waveplate at fourth order made with quartz is about 0.83 mm thick. Such a part is certainly easy to handle. However, as discussed in the previous section, the bandwidth of such a high-order plate unsuitably low.

A true zero-order waveplate is the thinnest plate possible that meets the target retardation (Fig. 4.18(b)). The thickness of a true zero-order half-wave and quarter-wave waveplate made in crystalline quartz is $L_{\lambda/2} \simeq 92$ μm and $L_{\lambda/4} \simeq 46$ μm at 1.55 μm, respectively. It is hard to fixture and hold such thin plates, which until recently has made these plates expensive. However, optical contacting of quartz blanks to an optically flat fused silica block and one-side polishing of the blank eases the fixturing problem. The finished waveplate is removed by heating the block. Such waveplates can be very high quality and exhibit extinction ratios better than 55 dB.

A classic solution to the cost required to make a true zero-order plate is to make a compound zero-order plate (Fig. 4.18(c)). Here two thick quartz blocks are cemented or optically contacted with the extraordinary axes crossed. The difference in thickness determines the retardation. The two parts can be made arbitrarily thick as long as the difference is maintained. However, the compound zero-order waveplate is limited by the accuracy with which the birefringent axes can be crossed. Typical extinction ratios are no better than 27 dB.

The retardation produced by a compound zero-order plate is very sensitive to misalignment to the beam. The plate is zero-order not just at the center wavelength but when perpendicular to the beam. The angular aperture of the compound plate must be considered, and is much smaller than that of a true zero-order waveplate. Overlooking the effect of the angular aperture will lead to erroneous experimental results. Lastly, if the waveplate is to be rotated, the thickness of the compound waveplate will displace the beam if there is any wobble in the rotation. Programmable PMD sources are an example where the waveplates are mechanically rotated.

A very good option which is becoming more common today is to fabricate a true zero-order waveplate optically contacted to a permanent host such as BK7 (Fig. 4.18(d)). Typically a larger part is made and several waveplates with hosts are separated by dicing. Optical contacting is the process of bonding two highly polished glass surfaces together using van der Waals force and is the preferred method, as cement bonding causes undesired reflections at the interface. To strengthen the contact, the parts are annealed to make them inseparable. The hosted true zero-order waveplate allows the part to be handled and fixed into location with ease.

Finally, a bi-crystalline waveplate achromat can be made with materials having complementary wavelength dispersions. The MgF_2/crystalline quartz achromat is one example (Fig. 4.18(e)). As both crystalline quartz and MgF_2 are positive uniaxial crystals, the birefringent axes are necessarily crossed. The difference in thickness–index product sets the net retardation [19].

4.6.3 Waveplate Combinations

Waveplate combinations can be used to create a variety of effects such as waveplate achromats or polarization controllers. Below are three important examples of waveplate combinations: the Evans phase shifter, the Pancharatnam achromat, and the Shirasaki achromat. Each combination uses multiple waveplates of various retardations and orientations to achieve a particular result. Not presented below but of some importance is the Koester stacked half-wave achromat [34]. Dynamic polarization control in elementary form is left to §4.6.4.

The Evans Phase Shifter

The Evans phase shifter [20] mechanically imparts a precession on an input polarization state, about an associated principal axis, that is equivalent to a change in frequency. Evans originally applied the phase shifter to tune a Lyot filter designed for astronomical observations. Other demonstrations have shown further application to astronomy [6], to interleavers [8], and to PMD sources [17].

The phase shifter, illustrated in Fig. 4.19, is a three-element combination of quarter-, half-, and quarter-wave waveplates. The equivalent birefringent

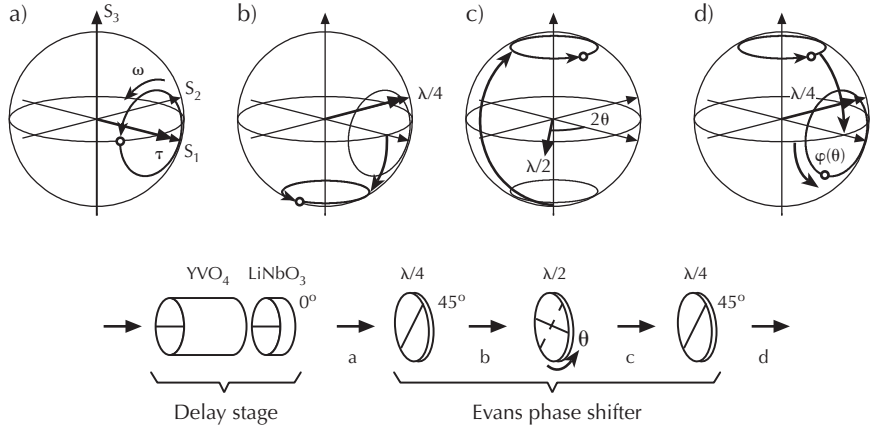

Fig. 4.19. Evans phase shifter. Quarter-, half-, quarter-wave waveplate combination, with outer plates fixed and center plate rotatable, tunes the birefringent phase of the adjacent principal waveplates. The quarter-wave plates are fixed at $+45°$ with respect to the principal waveplate. In Stokes space: a) locus of output SOP from principal plates over frequency; open circle denotes one frequency. b) Quarter-wave transformation to lower pole. c) Half-wave transformation to upper pole and mirror image about birefringent axis. d) Quarter-wave transformation back to principal waveplate axis. The change in open-circle position is equivalent to a frequency change. The null position of the tuning plate is at $-45°$ with respect to the principal axis.

axis of the combination is called the principal axis. The phase shifter can be located adjacent to a highly multi-order delay stage (such as the YVO_4-$LiNbO_3$ stage, as illustrated) and will tune the birefringent phase of the stage when the principal axis of the phase shifter is aligned to the birefringent axis of the delay.

In the phase shifter, the two quarter-wave waveplates are aligned and their axes are further rotated by 45° with respect to the principal axis. The half-wave waveplate, called the tuning plate and located between the two quarter-wave waveplates, controls the birefringent phase of the cascade. The null position of the tuning plate is at $-45°$ with respect to the principal axis. A rotation of the tuning plate is tantamount to a shift of the birefringent phase. Jones calculus shows that the quarter-, half-, quarter-waveplate cascade combines as

$$\frac{1}{2}\begin{pmatrix} 1 & -j \\ -j & 1 \end{pmatrix}\begin{pmatrix} \cos 2\theta_\varphi & \sin 2\theta_\varphi \\ \sin 2\theta_\varphi & -\cos 2\theta_\varphi \end{pmatrix}\begin{pmatrix} 1 & -j \\ -j & 1 \end{pmatrix} = \begin{pmatrix} \mathrm{e}^{-j2\theta_\varphi} & 0 \\ 0 & -\mathrm{e}^{j2\theta_\varphi} \end{pmatrix} \quad (4.6.16)$$

where the first and third Jones matrices describe the quarter-wave waveplates at +45° and the second Jones matrix describes the half-wave waveplate rotated by physical angle θ_φ. The resultant matrix shows a net birefringent phase plus a mirror image taken about the principal axis. The total birefringent phase of the delay and phase shifter is

$$\varphi(\omega, \theta_\varphi) = \omega\tau_s + (4\theta_\varphi - \pi) \tag{4.6.17}$$

The action of the Evans phase shifter in Stokes space is illustrated in Fig. 4.19. While the phase shifter can endlessly and continuously tune the birefringent phase of the cascade, there is no significant delay through the shifter. Endless rotation creates endless frequency shift (of the periodic spectrum) but without change in free-spectral range.

The Pancharatnam Achromat

Pancharatnam [5, 39] determined the conditions under which three waveplates can be combined so that the equivalent birefringent axis lies in the equatorial plane and the equivalent retardation is a prescribed value. His work can be reduced to the Evans phase shifter, which he briefly described and seems to have developed independently, but is more generally used to build achromatic retardation plates such as quarter-wave achromats. The Pancharatnam has a direct analogue to cascaded Mach-Zehnder interferometers uses in integrated optics to form achromatic waveguide-waveguide couplers [10]. The Pancharatnam and waveguide achromats were invented independently.

The Pancharatnam achromat is constructed with three waveplates, a first and last waveplate having equal retardation and extraordinary axis orientation, and an intermediate waveplate having a possibly different retardation and orientation. In this case, any choice of retardation and orientation values keeps the principal axis of the combination on the equator. There are two steps for the achromatic calculation: a first step derives the retardation and principal axis of the combination, and a second calculation determines the achromatic behavior.

As a departure from Pancharatnam's derivation, spin-vector calculus in Jones form is used here to determine the governing equations. For first and third waveplates having orientation $\hat{r}_1$ and retardation φ_1, and a second waveplate having orientation $\hat{r}_2$ and retardation φ_2, the Jones operators are

$$U_{1,2} = \cos(\varphi_{1,2}/2)I - j(\hat{r}_{1,2} \cdot \vec{\sigma})\ \sin(\varphi_{1,2}/2) \tag{4.6.18}$$

As an aid to resolve the following operator product, the vector $\hat{r}_2$ is projected onto $\hat{r}_1$ and an orthogonal axis $\hat{r}_\perp$ as

$$\hat{r}_2 = \hat{r}_1\,(\hat{r}_2 \cdot \hat{r}_1) + \hat{r}_\perp\,(\hat{r}_2 \cdot \hat{r}_\perp) \tag{4.6.19}$$

and, for the following, $\hat{r}_2 \cdot \hat{r}_1 = \cos 2\theta_{21}$, as is customary. Using the spin-vector identities in §2.5.4, the waveplate combination is written

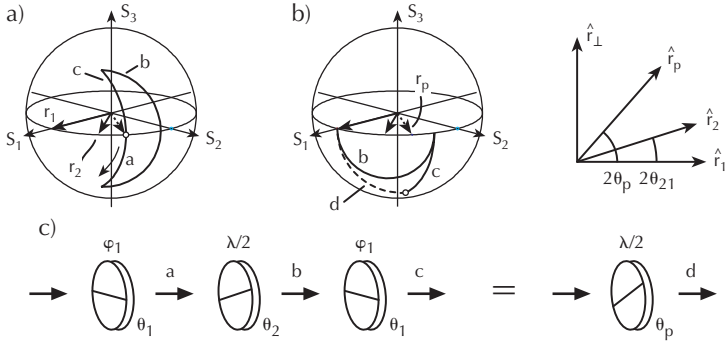

Fig. 4.20. Pancharatnam waveplate combination equivalent to single principal waveplate. a) Polarization evolution comparison, launched along eigen-axis of principal waveplate. Through combination, polarization first rotates along (a) about $\hat{r}_1$, then along (b) about $\hat{r}_2$, then returning along (c) about $\hat{r}_1$. b) Launch state along eigen-axis of $\hat{r}_1$. Through principal waveplate polarization rotates along (d) about $\hat{r}_p$. Through combination, polarization pirouettes about $\hat{r}_1$, rotates along (b) about $\hat{r}_2$, and rotates along (c) about $\hat{r}_1$. c) Equivalence between combination and principal waveplate; first and third waveplates of combination have same retardation and orientation.

$$\begin{aligned} U_1U_2U_1 = {} & \cos\varphi_1\cos(\varphi_2/2) - \cos 2\theta_{21}\sin\varphi_1\sin(\varphi_2/2) \\ & - j\,(\hat{r}_1\cdot\vec{\sigma})\sin\varphi_1\cos(\varphi_2/2) - j\,(\hat{r}_1\cdot\vec{\sigma})\cos 2\theta_{21}\cos\varphi_1\sin(\varphi_2/2) \\ & - j\,(\hat{r}_2\cdot\hat{r}_\perp)\,(\hat{r}_\perp\cdot\vec{\sigma})\sin(\varphi_2/2) \end{aligned} \quad (4.6.20)$$

Notice that there are no $\hat{s}_3$ components in (4.6.20); the principal axis of the combination lies in the equatorial plane.

The waveplate combination can be identified with a single principal waveplate U_p,

$$U_p = \cos(\varphi_p/2)I - j\,(\hat{r}_p\cdot\vec{\sigma})\sin(\varphi_p/2) \quad (4.6.21)$$

Making identification with (4.6.20), the principal retardation φ_p is

$$\cos(\varphi_p/2) = \cos\varphi_1\cos(\varphi_2/2) - \cos 2\theta_{21}\sin\varphi_1\sin(\varphi_2/2) \quad (4.6.22)$$

and the principal axis θ_p is

$$\cot(2\theta_p) = \csc(2\theta_{21})\,(\sin\varphi_1\cot(\varphi_2/2) + \cos 2\theta_{21}\cos\varphi_1) \quad (4.6.23)$$

where, in the latter case, the arc cotangent between the orthogonal $(\hat{r}_1\cdot\vec{\sigma})$ and $(\hat{r}_\perp\cdot\vec{\sigma})$ axes was taken. Equations (4.6.22-4.6.23) are the two main results first derived by Pancharatnam.

The equivalence between a single waveplate and a Pancharatnam combination is illustrated in Fig. 4.20. There the polarization transformation through a principal waveplate and an equivalent combination of three plates, where the

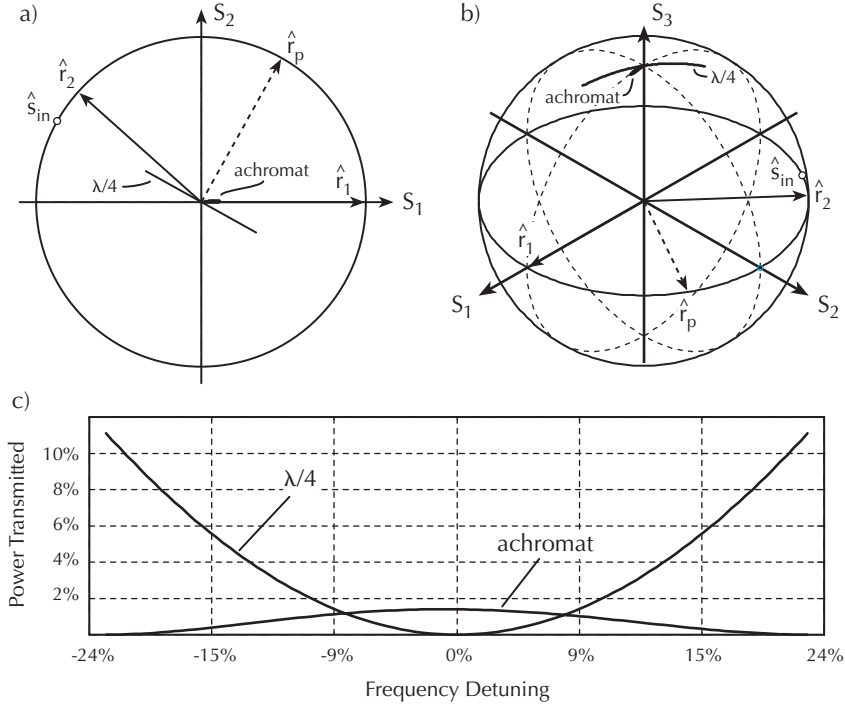

Fig. 4.21. Realization of a Pancharatnam achromat: $\varphi_p = \pi/2$, $\varphi_1 = 116.2°$, $\varphi_2 = \pi$, $\theta_{21} = 69.1°$ physical angle, $\theta_p = 30.3°$ physical angle. a) Comparison of single $\lambda/4$ waveplate (principal axis dotted) and achromatic waveplate (extraordinary axes solid) over detuning range $\epsilon = \pm 25\%$, projected on Stokes space in plan view. Achromat shows tighter progression than single plate. b) Different view of same, input state rotated to top pole. c) Comparison of transmitted power through polarizer oriented along $\hat{s}_1$ for single plate and achromat.

center plate is half-wave, is illustrated. Note the distinctly different contours that are traced and yet the output states are the same in either case.

The Pancharatnam combination supports enough degrees of freedom to implement a waveplate combination that is less chromatically dependent than a single waveplate. This is called the Pancharatnam achromat. Consider a frequency deviation such that

$$\varphi \pm \delta\varphi = (1 \pm \epsilon)\varphi \tag{4.6.24}$$

The detuning will also be written as $\varphi^{\pm}$ until later expansion. The equations that define the solution require the same principal retardation and axis at $\varphi^{\pm}$:

$$\cos 2(\varphi_p/2) = \cos\varphi_1^+ \cos(\varphi_2^+/2) - \sin\varphi_1^+ \sin(\varphi_2^+/2)\cos 2\theta_{21} \tag{4.6.25a}$$

$$\cos 2(\varphi_p/2) = \cos\varphi_1^- \cos(\varphi_2^-/2) - \sin\varphi_1^- \sin(\varphi_2^-/2)\cos 2\theta_{21} \tag{4.6.25b}$$

$$\sin\varphi_1^+ \cot(\varphi_2^+/2) + \cos\varphi_1^+ \cos 2\theta_{21} = \cot(\varphi_2^-/2)\sin\varphi_1^- + \cos 2\theta_{21}\cos\varphi_1^- \tag{4.6.25c}$$

After some cumbersome manipulations and setting the center waveplate to half-wave retardation $\varphi_2 = \pi$, the retardation of the outer two plates satisfies the equation

$$\sin\epsilon\varphi_1 = \frac{\sin(\epsilon\pi/2)}{\cos(\varphi_p/2)}\ \sin\varphi_1 \tag{4.6.26}$$

The inclination of the center waveplate with respect to the outer plates is

$$\cos 2\theta_{21} = -\frac{\tan(\epsilon\pi/2)}{\tan(\epsilon\varphi_1)} \tag{4.6.27}$$

Lastly, the inclination of the principal axis is calculated from

$$\sin 2\theta_{21}\cot 2\theta_p = \sin(1-\epsilon)\varphi_1 \tan(\epsilon\pi/2) + \cos(1-\epsilon)\varphi_1 \cos 2\theta_{21} \tag{4.6.28}$$

Inspection of (4.6.26) shows that the possible achromatic bandwidth depends on the principal retardation. A half-wave retardation cannot be achromatic while a quarter-wave retardation exhibits the broadest possible range. For this reason the Pancharatnam achromatic is typically quarter-wave. Note, however, that (4.6.26–4.6.28) are derived for $\varphi_2 = \pi$; relaxation of this parameter allows more complexity and, in particular, a achromatic half-wave combination.

Figure 4.21(a,b) shows a Stokes-space comparison between a quarter-wave waveplate and an achromat designed to cover a detuning of $\epsilon = \pm 25\%$. As illustrated, a polarization state on the equator transformed through the achromat traces a tight loop about $\hat{s}_3$. In contrast, the same state through the quarter-wave waveplate traces a unidirectional arc through $\hat{s}_3$ as is expected from simple precession. Figure 4.21(c) shows the output states as transmitted through a polarizer. Again the bandwidth of the achromat is substantially broader than the single waveplate.

The Shirasaki Achromat

The Shirasaki achromat [55] compensates to first order the frequency dependence of a Faraday rotator (or optically active) waveplate for a particular input state of polarization. The input state is known in components such as optical isolators and circulators. A Faraday rotator waveplate precesses an input state of polarization about the $\pm\hat{s}_3$ axis, the sign determined by the relation between the magnetization vector and the propagation direction. Table 4.8 on page 207 lists Jones and Stokes operators for Faraday rotation.

One realization of the achromat, illustrated in Fig. 4.22(a), is constructed with a half-wave and then quarter-wave waveplate, followed by the Faraday

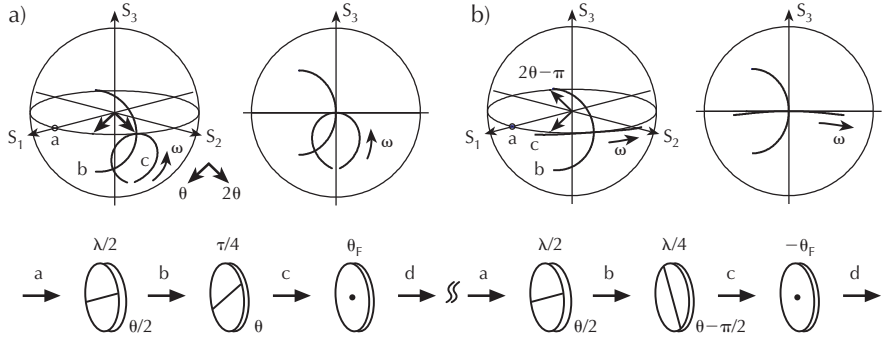

Fig. 4.22. Two realizations of the Shirasaki achromat: Half-wave waveplate followed by a quarter-wave waveplate, the combination preceding a Faraday rotator. a) Waveplates are oriented at $\theta/2$ and θ, where $\theta = 30°$. To first order, the Stokes view shows frequency-dependent motion counter to that of a $+\hat{s}_3$-oriented Faraday rotator. To second order the contour curvatures of the waveplates add, reducing the bandwidth. b) Quarter-wave waveplate rotated by $-90°$ from a). Curvatures largely cancel and the bandwidth is increased. The transformation motion runs counter to a), requiring a reversed orientation of the Faraday rotator.

rotator. The extraordinary axis of the half-wave plate is rotated by $\theta/2$ from the horizontal while that of the quarter-wave plate is rotated by θ. The input state of polarization is expected to be linear and along the horizontal $+\hat{s}_1$. All three plates change retardation to first order with frequency; denote the changes as $\delta\varphi_F$, $\delta\varphi_{\lambda/4}$, and $\delta\varphi_{\lambda/2}$ for the Faraday, quarter-wave, and half-wave plates, respectively.

In Stokes space, the half-wave waveplate rotates the horizontal input polarization to another point on the equator, the angle of separation being 2θ. Considering small changes in frequency, the locus of polarization states forms a line perpendicular to the equator, to first order. The quarter-wave waveplate, whose birefringent axis is at 2θ, rotates the locus parallel to the equator. The achromat generates a state on the equator at 2θ that moves toward $+\hat{s}_1$ with increased frequency. This motion is counter to that of a Faraday rotator having its orientation along $+\hat{s}_3$, which rotates the polarization state toward $-\hat{s}_1$ with increased frequency. These two motions can cancel.

A rigorous analysis is easily done with spin-vector operators. Stokes operators are constructed for each plate and expanded to include first-order frequency deviation. The first-order operators are

$$R_F + \delta R_F = \hat{s}_3(\hat{s}_3\cdot) + (\hat{s}_3\times) + \delta\varphi_F(\hat{s}_3 \times \hat{s}_3\times) \tag{4.6.29a}$$

$$R_{\lambda/4} + \delta R_{\lambda/4} = \hat{r}_4(\hat{r}_4\cdot) + (\hat{r}_4\times) + \delta\varphi_4\,(\hat{r}_4(\hat{r}_4\cdot) - I) \tag{4.6.29b}$$

$$R_{\lambda/2} + \delta R_{\lambda/2} = 2\hat{r}_2(\hat{r}_2\cdot) - I - \delta\varphi_2(\hat{r}_2\times) \tag{4.6.29c}$$

where the birefringent vectors $\hat{r}_2$ and $\hat{r}_4$ lie in the equatorial plane. To first order, a frequency change is expanded as

$$\delta\left(R_F R_{\lambda/4} R_{\lambda/2}\right) \simeq (\delta R_F) R_{\lambda/4} R_{\lambda/2} + R_F (\delta R_{\lambda/4}) R_{\lambda/2} + R_F R_{\lambda/4} (\delta R_{\lambda/2}) \tag{4.6.30}$$

Interestingly, the second term on the right-hand side vanishes because $\hat{r}_4$ is aligned to the nominal polarization state produced by $R_{\lambda/2}$. When the operator (4.6.30) is applied to state $\hat{s}_1$ the contributing difference terms evaluate to

$$(\delta R_F) R_{\lambda/4} R_{\lambda/2} = \delta\varphi_F \left(\hat{s}_3 \times \hat{s}_3 \times\right) \left(\hat{s}_1 \cos 2\theta + \hat{s}_2 \sin 2\theta\right) \tag{4.6.31a}$$

$$R_F R_{\lambda/4} (\delta R_{\lambda/2}) = \delta\varphi_{\lambda/2} \sin\theta \left(\hat{s}_3 (\hat{s}_3 \cdot) + (\hat{s}_3 \times)\right) \left(\hat{s}_1 \sin 2\theta - \hat{s}_2 \cos 2\theta\right) \tag{4.6.31b}$$

By completing the vector products and setting the result to zero, a simple relation between frequency deviations of the Faraday and half-wave plates is found

$$\delta\varphi_F = \delta\varphi_{\lambda/2} \sin 2\theta \tag{4.6.32}$$

This relation makes physical sense because the precession rates need to be matched. The half-wave waveplate has a $\sin\theta$ multiplier because the radius of the precession circle depends on the angle between the input state and the extraordinary axis. In light of (4.6.13), the Stokes angle 2θ is defined by

$$\sin 2\theta = \frac{\varphi_F}{\varphi_{\lambda/2}} \tag{4.6.33}$$

In the case of an isolator, $\varphi_F = \pi/2$. Accordingly, the physical angles for the waveplates are $\theta_{\lambda/2} = 15°$ and $\theta_{\lambda/4} = 30°$. To maximize the second-order bandwidth, the waveplates should be made true zero-order.

Another consideration is necessary when analyzing the achromat to second order. As illustrated in Fig. 4.22(a) the curvature of states can add, which reduces the achromatic bandwidth. As an alternative, Fig. 4.22(b) illustrates the same achromat with the quarter-wave waveplate rotated by a 90°, which is tantamount to exchange of the ordinary and extraordinary axes. In this case the curvature of states imparted by the half-wave and quarter-wave waveplates subtract, providing a very broad band over which the combination is achromatic. When the quarter-wave plate is oriented like this, the state motion with increasing frequency is opposite that of the origin configuration. The Faraday rotator must be accordingly reversed. Whether the quarter-wave waveplate is to be rotated an additional 90° depends on θ: if $\theta_{\lambda/4} < 45°$ then the additional rotation is necessary, otherwise it is not.

4.6.4 Elementary Polarization Control

A polarization controller dynamically changes its transformation effect to either track an incoming state of polarization or alter the output state polarization in a programmed way. Although a polarization controller can be arbitrarily complex with enough waveplates, the fundamental question is how few waveplates are needed for certain transformations.

A particularly useful control is "arbitrary-to-arbitrary," wherein an arbitrary input polarization state is mapped to an arbitrary output state. Such a controller offers complete control. One subset is "linear-to-arbitrary," which is useful when the input comes from a laser. A strictly endless controller is built with parts that are themselves endlessly rotatable, like a birefringent-crystal waveplate mounted on a rotary stage. Other controller types provide an apparently endless transformation but do so either by "unwinding" or digitally "flipping" the elementary parts. As a example, liquid crystal birefringent elements have a limited voltage range, which inhibits endless control of any one element. The same applies for fiber squeezers that induce birefringence through stress. Theoretically, unwinding or digital flipping can create endless polarization control, but the algorithms rely on certainty of the element retardations, which in practice is rarely the case. An extensive review of polarization control can be found in [60].

The elementary controllers considered in this section are built with a cascade of birefringent waveplates. These plates are physical pieces that have a fixed retardation and variable angle, although the birefringent axis is constrained to the equatorial plane. A common alternative in the industry is the lithium-niobate electro-optic polarization controller [26, 59]. Both birefringent and electro-optic controllers are strictly endless, and the electro-optic controllers can actuate in the megahertz range or higher. Also, unlike the birefringent waveplates, the bias voltage on a electro-optic controller can be changed as well as the orientation voltage, which changes the retardation. A polarization controller that combines effects of waveplate rotation and retardation modulation is called a hybrid controller.

Before doing an analysis of waveplate combinations, it should be obvious that a single fixed-retardation waveplate element cannot make arbitrary transformations. The only possible transformation type through a single waveplate is when the cross-product between the input state and desired output state lies on the equator, so that the birefringent axis can point in that direction, and the dot-product between the states is equal to the retardation of the plate.

Figure 4.23 illustrates transformations through single quarter- and half-wave waveplates over a full revolution of the plates for a fixed input state. Figures 4.23(a,b) illustrate the "bow-tie" pattern created by a quarter-wave waveplate at a fixed frequency, while Figures 4.23(c,d) show the constant-latitude pattern created by a half-wave waveplate. In particular note that a quarter-wave waveplate can transform a circular state to a linear state and back, while a half-wave waveplate maps linear states to linear and circular states to circular.

$\lambda/4, \lambda/4$ Arbitrary-To-Arbitrary Control

Two independently adjustable quarter-wave waveplates are the minimum requirement for arbitrary-to-arbitrary polarization transformation. To show that two quarter-wave plates with variable extraordinary axis inclination

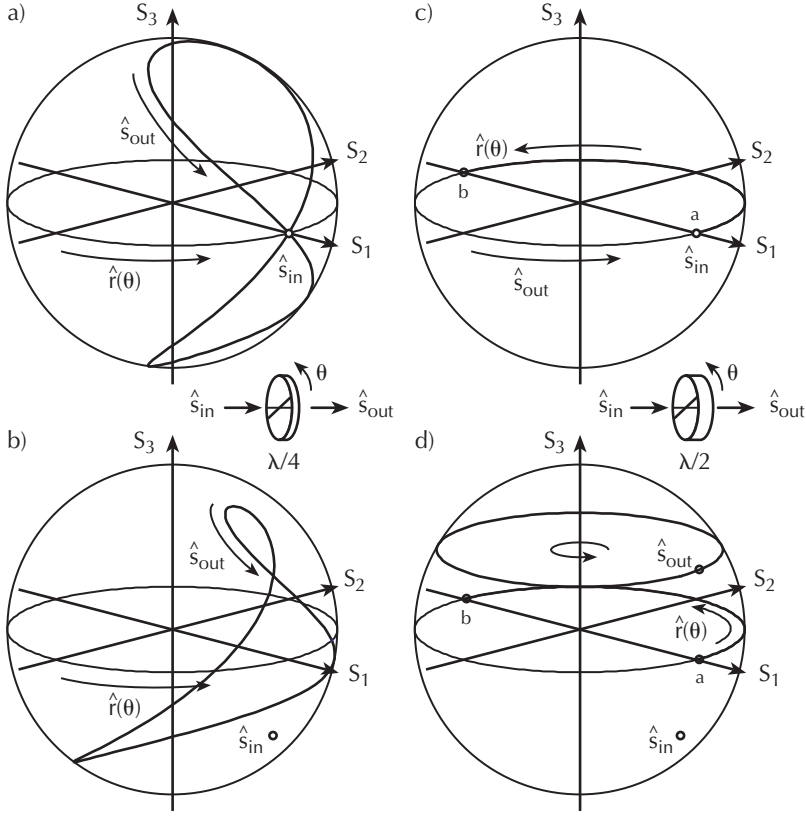

Fig. 4.23. Polarization control for single quarter- and half-wave waveplates. Trajectories show output locus for a fixed input over full revolution of the respective birefringent waveplate (shown in inset). a) "Bow-tie" locus traced by a quarter-wave plate for horizontal linear input polarization. b) Distorted bow-tie for elliptical input polarization. c) Line-of-latitude locus traced by a half-wave plate for horizontal (or any) linear input polarization. d) Elevated line-of-latitude for elliptical input polarization. Note the eccentricity does not change.

(Fig. 4.24(a)) can map any arbitrary polarization state to another arbitrary state, it is sufficient to show that orthogonal input states, such as along $\hat{s}_1$, $\hat{s}_2$, and $\hat{s}_3$, can each be mapped anywhere in Stokes space. An arbitrary input state can then be composed of these orthogonal states without violation of the mapping.

Recall that the Stokes operator for a quarter-wave plate is

$$R_{\lambda/4} = (\hat{r}\hat{r}\cdot) + (\hat{r}\times) \tag{4.6.34}$$

Two quarter waveplates in cascade generates the operator

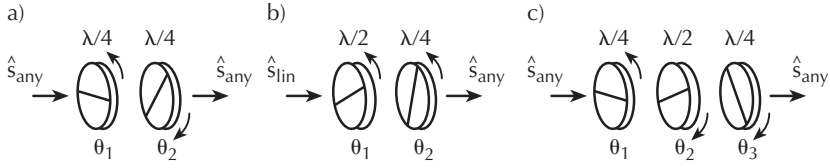

Fig. 4.24. Illustration of three birefringent waveplate polarization controllers. Each plate can be rotated independently. a) Quarter-, quarter-wave waveplate combination. Can map arbitrary-to-arbitrary polarization states. b) Half-, quarter-wave waveplate combination. Can map linear-to-arbitrary states. c) Quarter-, half-, quarter-wave waveplate combination. Can map arbitrary-to-arbitrary states.

$$\begin{aligned} R_2R_1 &= \hat{r}_2(\hat{r}_2\cdot\hat{r}_1)(\hat{r}_1\cdot) + \hat{r}_2(\hat{r}_2\cdot\hat{r}_1\times) + \hat{r}_2\times\hat{r}_1(\hat{r}_1\cdot) + \hat{r}_2\times\hat{r}_1\times \\ &= \hat{r}_2\left[\cos\theta_{21}(\hat{r}_1\cdot) - \sin\theta_{21}(\hat{s}_3\cdot)\right] + (\hat{r}_2\times\hat{r}_1\times) - \hat{s}_3\sin\theta_{21}(\hat{r}_1\cdot) \end{aligned} \quad (4.6.35)$$

Operating on three orthogonal input states, the output states are

$$R_2R_1\hat{s} = \begin{cases} \hat{r}_2\left(\cos\theta_{21}\cos\theta_{1s}\right) + \hat{r}_\perp\left(\sin\theta_{1s}\right) - \hat{s}_3\left(\sin\theta_{21}\cos\theta_{1s}\right) & \hat{s}=\hat{s}_1 \\ \hat{r}_2\left(\cos\theta_{21}\sin\theta_{1s}\right) - \hat{r}_\perp\left(\cos\theta_{1s}\right) - \hat{s}_3\left(\sin\theta_{21}\sin\theta_{1s}\right) & \hat{s}=\hat{s}_2 \\ -\hat{r}_2\left(\sin\theta_{21}\right) - \hat{s}_3\left(\cos\theta_{21}\right) & \hat{s}=\hat{s}_3 \end{cases} \quad (4.6.36)$$

where θ_{1s} is the angle between the associated vector and $\hat{s}_1$, and where, as a variation on (4.6.19),

$$\hat{r}_1 = \hat{r}_2\left(\hat{r}_1\cdot\hat{r}_2\right) + \hat{r}_\perp\left(\hat{r}_1\cdot\hat{r}_\perp\right) \quad (4.6.37)$$

By definition, $\hat{r}_\perp$ is a perpendicular axis in the equatorial plane such that $\hat{r}_2\cdot\hat{r}_\perp = 0$ and $\hat{r}_2\times\hat{r}_\perp = \hat{s}_3$.

Consider the transformation of $\hat{s}_1$. The coefficients to $\hat{r}_2$, $\hat{r}_\perp$, and $\hat{s}_3$ can each independently span the range $[-1,1]$, provided a judicious choice of θ_{21} and θ_{1s} is made. Therefore R_2R_1 can map $\hat{s}_1$ to anywhere in Stokes space. The same argument applies to transformations of $\hat{s}_2$ and $\hat{s}_3$. In the latter case note that the direction of $\hat{r}_2$ is arbitrary: the linear component of the output polarization can be arbitrarily oriented.

Since an arbitrary input state is a linear combination of projections onto orthogonal axes, the linearity of R_2R_1 ensures that any such input state can be mapped to an arbitrary output state.

$\lambda/2, \lambda/4$ Linear-To-Arbitrary Control

A half-wave plate followed by a quarter-wave plate (Fig. 4.24(b)), can transform any linear input state to an arbitrary output state. To show this, recall that the Stokes operator for a half-wave plate is

$$R_{\lambda/2} = 2\left(\hat{r}\hat{r}\cdot\right) - I \quad (4.6.38)$$

The half-wave (R_2'), quarter-wave (R_1) cascade generates the operator

$$\begin{aligned} R_2' R_1 &= 2\hat{r}_2(\hat{r}_2 \cdot \hat{r}_1)(\hat{r}_1 \cdot) - \hat{r}_1(\hat{r}_1 \cdot) + 2\hat{r}_2(\hat{r}_2 \cdot \hat{r}_1 \times) - \hat{r}_1 \times \\ &= 2\hat{r}_2 \left[\cos\theta_{21}(\hat{r}_1 \cdot) - \sin\theta_{21}(\hat{s}_3 \cdot)\right] - \hat{r}_1(\hat{r}_1 \cdot) - (\hat{r}_1 \times) \end{aligned} \tag{4.6.39}$$

Operating on three orthogonal input states, the output states are

$$R_2' R_1 \hat{s} = \begin{cases} \hat{r}_2 \left(\cos\theta_{21} \cos\theta_{1s}\right) - \hat{r}_\perp \left(\sin\theta_{21} \cos\theta_{1s}\right) - \hat{s}_3 \left(\sin\theta_{1s}\right) & \hat{s} = \hat{s}_1 \\ \hat{r}_2 \left(\cos\theta_{21} \sin\theta_{1s}\right) - \hat{r}_\perp \left(\sin\theta_{21} \sin\theta_{1s}\right) - \hat{s}_3 \left(\cos\theta_{1s}\right) & \hat{s} = \hat{s}_2 \\ -3\hat{r}_2 \left(\sin\theta_{21}\right) + \hat{r}_\perp \left(\cos\theta_{21}\right) & \hat{s} = \hat{s}_3 \end{cases} \tag{4.6.40}$$

As in the case of cascaded quarter-wave waveplates, input states $\hat{s}_1$ and $\hat{s}_2$ can be mapped arbitrarily. However, not so for a launch along $\hat{s}_3$. In that case the half-, quarter-wave pair only maps to the equator; any remaining component along $\hat{s}_3$ vanishes. This makes physical sense because a circular state that transits a half-wave plate is rotated to the orthogonal circular state. The quarter-wave plate in turn rotates the resultant circular state to the equator.

The half-wave, quarter-wave cascade transforms any linear state to an arbitrary state. In the opposite direction, any arbitrary state can be mapped to a linear state. This may be useful when the light is subsequently analyzed by a polarizer.

$\lambda/4, \lambda/2, \lambda/4$ Arbitrary-To-Arbitrary Control

The same procedure is used to analyze the cascade of quarter-, half-, quarter-wave waveplates. To aid with the reductions, $\hat{r}_3 \cdot \hat{r}_{3\perp} = 0$ and $\hat{r}_3 \times \hat{r}_{3\perp} = \hat{s}_3$ define the vector $\hat{r}_{3\perp}$. The concatenated Stokes operator is

$$\begin{aligned} R_3 R_2' R_1 = {} & 2\hat{r}_3(\hat{r}_3 \cdot \hat{r}_2) \left(\cos\theta_{21}(\hat{r}_1 \cdot) - \sin\theta_{21}(\hat{s}_3 \cdot)\right) \\ & - \hat{r}_3(\hat{r}_3 \cdot \hat{r}_1)(\hat{r}_1 \cdot) - \hat{r}_3(\hat{r}_3 \cdot \hat{r}_1 \times) \\ & + 2(\hat{r}_3 \times \hat{r}_2) \left(\cos\theta_{21}(\hat{r}_1 \cdot) - \sin\theta_{21}(\hat{s}_3 \cdot)\right) \\ & - (\hat{r}_3 \times \hat{r}_1)(\hat{r}_1 \cdot) - (\hat{r}_3 \times \hat{r}_1 \times) \end{aligned} \tag{4.6.41}$$

Transformation of the three orthogonal input states generates the following expressions:

$$\begin{aligned} R_2 R_2' R_1 \hat{s}_1 &= \hat{r}_3 \cos(\theta_{32} - \theta_{21}) \cos\theta_{1s} - \hat{r}_{3\perp} \sin\theta_{1s} - \hat{s}_3 \sin(\theta_{32} - \theta_{21}) \cos\theta_{1s} \\ R_2 R_2' R_1 \hat{s}_2 &= \hat{r}_3 \cos(\theta_{32} - \theta_{21}) \sin\theta_{1s} + \hat{r}_{3\perp} \cos\theta_{1s} - \hat{s}_3 \sin(\theta_{32} - \theta_{21}) \sin\theta_{1s} \\ R_2 R_2' R_1 \hat{s}_3 &= \hat{r}_3 \sin(\theta_{32} - \theta_{21}) + \hat{s}_3 \cos(\theta_{32} - \theta_{21}) \end{aligned}$$

As was the case with two quarter-wave waveplates, the output polarization for each orthogonal input is mapped arbitrarily in Stokes space provided a judicious choice of waveplate angles.

In comparison to (4.6.36), the present transformation makes the angle substitution $\theta_{21} \mapsto (\theta_{32} - \theta_{21})$. The addition of the intermediate half-wave plate provides a degree of freedom not available for the quarter-wave pair, wherein the value of $(\theta_{32} - \theta_{21})$ can be changed without simultaneous change of $\hat{r}_3$, $\sin\theta_{1s}$, or both. For this reason the quarter-, half-, quarter-wave combination is often preferred over the lone pair.

4.6.5 TIR Polarization Retarders

A total-internal reflection retarder is nearly achromatic and accordingly has practical application in components and instruments. As analyzed in §3.5.6, total internal reflection retards light due to the difference of evanescent field decay between TE and TM plane waves. While the retardation of a waveplate is directly proportional to frequency (4.6.1), the frequency dependence of TIR retardation is governed by the material dispersion alone. Indeed, differentiation of the retardance expression (3.5.47) on page 103 with respect to frequency yields

$$\frac{d\varphi}{d\omega} = \frac{2u}{u^2+1} \frac{1}{n(\omega)\left(n^2(\omega)\sin^2\theta - 1\right)} \frac{dn(\omega)}{d\omega} \tag{4.6.42}$$

where

$$u = \frac{\cos\theta\sqrt{n^2(\omega)\sin^2\theta - 1}}{n(\omega)\sin^2\theta} \tag{4.6.43}$$

Selection of a low-dispersion material will produce a highly achromatic retarder.

A common TIR retarder is the Fresnel rhomb, illustrated in Fig. 4.25(a). The Fresnel rhomb is designed to convert linearly polarized light of the proper inclination to circular polarization after two reflections while maintaining the output co-linear with the input. The three design parameters are the retardance φ per TIR, the rhombohedral angle θ, and the material index n. Association of physical space to Stokes space is made by referencing the Stokes axis $\hat{s}_1$ to the TE direction on the plane of incidence. Since $\hat{s}_1$ is also associated with the positive eigenvector of the Jones operator U, the retardance expression

$$\varphi = 2\tan^{-1} u \tag{4.6.44}$$

follows a right-hand precession rule about $\hat{s}_1$. Accordingly, linearly polarized light aligned to $+\hat{s}_2$ is transformed to circular polarization $\hat{s}_3$ when $\varphi = \pi/2$.

The practical design of a Fresnel rhomb should minimize the retardance sensitivities to frequency and incident angle. The frequency sensitivity is given above, and the angular sensitivity of total internal reflection retardance is

$$\frac{d\varphi}{d\theta} = \frac{2u}{u^2+1} \frac{2 - \left(n^2+1\right)\sin^2\theta}{\sin\theta\cos\theta\left(n^2\sin^2\theta - 1\right)} \tag{4.6.45}$$

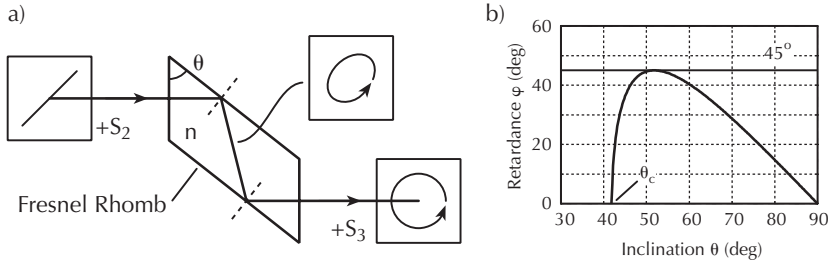

Fig. 4.25. A Fresnel rhomb can transform linear 45° polarization into circular polarization over a bandwidth limited only by material dispersion. a) Illustration of the rhomb, where two total-internal reflections impart a combined quarter-wave shift. b) Retardance of the rhomb as a function of apex angle θ, where $n = 1.497$. Retardance is zero at the critical angle and glacing angle. The retardance is 45° at $\theta = 51.8°$ while the first-order retardance sensitivity to input angle, by design, vanishes.

The angular sensitivity vanishes for

$$\sin\theta_o = \sqrt{\frac{2}{n^2+1}} \tag{4.6.46}$$

The angle θ_o also yields the maximum retardance for a given index n. Substitution of (4.6.46) into (4.6.43) gives the maximum u values for a given n:

$$u_{\max} = \frac{n^2-1}{2n} \tag{4.6.47}$$

For example, a lead-doped glass having index $n \sim 1.8$ generates a retardance per TIR of $\varphi \sim 64°$. As $\varphi = 90°$ is necessary for linear to circular conversion, the Fresnel rhomb typically uses two reflections to accumulate the full $\pi/2$ retardance.

To minimize the angular sensitivity while $\varphi = \pi/4$, the value of u is determined from (4.6.44) and the associated index n is calculated from (4.6.47). Figure 4.25(b) plots the retardance for a single reflection as a function of angle for this solution. The angular sensitivity vanishes just at the point of eighth-wave shift.

Beyond the elementary analysis presented here, two complete studies of rhomb sensitivities can be found in [4, 42]. Also, reference [9] applies TIR prisms to isolators and circulators to greatly extend their bandwidth; however the implementations are not particularly practical.

Separate from Fresnel rhombs, high-sensitivity magneto-optic sensors can use turning prisms to complete an optical circuit around a conductor [40]. When the light transits one or more unsaturated iron-garnet Faraday rotator elements located in proximity to the conductor, the Faraday rotation is proportional to the current-induced magnetic field. For such sensors, retardance

generated by the prisms reduces the small-signal sensitivity [41]. While the retardance per reflection can be reduced by bringing the incidence angle close to the critical angle, as can be seen in Fig. 4.25(b), the error sensitivities become impractically large. To overcome this limitation, a specially designed thin-film coating can be applied to the hypotenuse of the prism to reduce the retardance while remaining away from the critical angle. Reference [43] cites a design where the retardance was reduced to 1° at 1.3 μm and the retardance remained within 6° for a ±5° angular error.

4.7 Single and Compound Prisms

Prisms are a cornerstone of birefringent optical components. Simple isotropic prisms are used as turning prisms to bend the light 90° or 180° within a component, or as straightening prisms to compensate for the angular divergence between two beams emergent from a dual-fiber collimator. Birefringent prism pairs are used in isolators to create polarization diversity. Compound prisms such as the Wollaston, Rochon, and Kaifa prisms are used in many circulator designs for polarization diversity and angular compensation for dual-fiber collimators. The prisms studied in this section are designed in the small-angle limit, where Snell's law may be linearly approximated. A broad range of prisms is discussed in [24].

The isotropic isosceles prism illustrated in Fig. 4.26(a) has an apex angle α and refractive index n which, in general, is a function of wavelength. For a given angle of incidence θ_{in} on one face of the prism, the deflection angle β is

$$\beta = \theta_1 - \alpha + \sin^{-1}\left(\sin\alpha\sqrt{n^2 - \sin^2\theta_1} - \cos\alpha\sin\theta_1\right) \tag{4.7.1}$$

The angle of minimum deviation is that θ_1, or θ_{m}, which minimizes β. While the expression is complicated in the general case, minimum deviation requires symmetry between the input and output angles: $\theta_1 = \theta_4$.

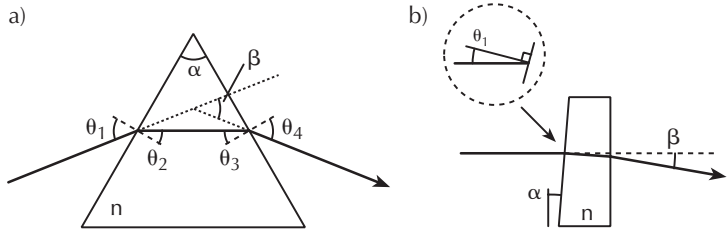

Fig. 4.26. Isosceles and small-angle prisms. a) Isosceles prism with apex angle α and refractive index n. Prism deflects input beam by angle β. b) Small-angle prism with near-normal incidence. For small angles $\beta = (n-1)\alpha$. This shape is also called a wedge prism.

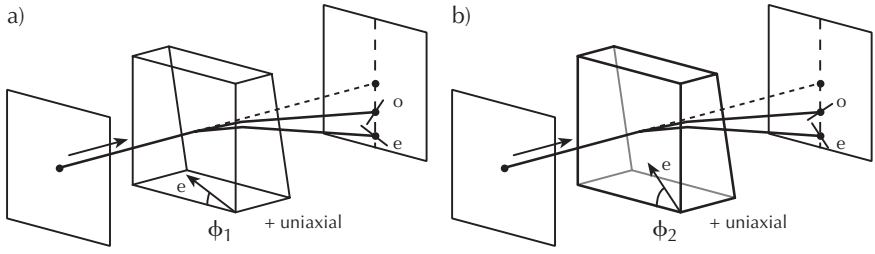

Fig. 4.27. Birefringent prisms having extraordinary axis perpendicular to input beam. The deflection of the beam is polarization dependent. For a (+) uniaxial crystal the polarization aligned to the extraordinary axis is deflected more than that aligned to the ordinary axis. The output polarization states are aligned to the ordinary and extraordinary axes of the prism. Deflection and output polarization states are independent. a) e axis tilted at angle ϕ_1. b) e axis tilted at angle ϕ_2.

For prisms with small apex angles and near-normal incidence (Fig. 4.26(b)), (4.7.1) is linearized to yield the deflection of a small-angle prism,

$$\beta \simeq (n-1)\,\alpha \tag{4.7.2}$$

The input angle for minimum deviation in this case is $\theta_{\mathrm{m}} = \alpha n$.

The birefringent prism is a prism made of birefringent crystalline material, typically uniaxial material. Birefringent prisms for isolators and most circulators are small angle prisms. A birefringent prism refracts like an isotropic prism and obeys (4.7.1), but the refractive index depends on the input polarization. In turn, the deflection is polarization dependent. Figure 4.27 illustrates two birefringent prisms made of the same material and having the same apex angle. The difference between the two prisms is the orientation of the extraordinary axis. For positive uniaxial material, the e-ray deflects more than the o-ray. The linear polarization states of the two output beams are aligned to the ordinary and extraordinary axes of the prism. The e-axis orientation determines the output polarization orientation but does not contribute to the deflection.

The following studies detail birefringent prism pairs in Wollaston, Rochon, Kaifa, and Shirasaki configurations.

4.7.1 Wollaston and Rochon Prisms

The Wollaston and Rochon compound prisms are birefringent prism pairs that angularly separate orthogonal linear polarization states. The Wollaston type uses two prisms with the same apex angle and material, and the extraordinary axes are crossed (Fig. 4.28(a)). The line of contact between the two parts is the hypotenuse of the prisms, and the input and output faces are parallel to one another. The prism is generally oriented perpendicular to, or with a small tilt to, the input beam. Two beams emerge from the compound prism,

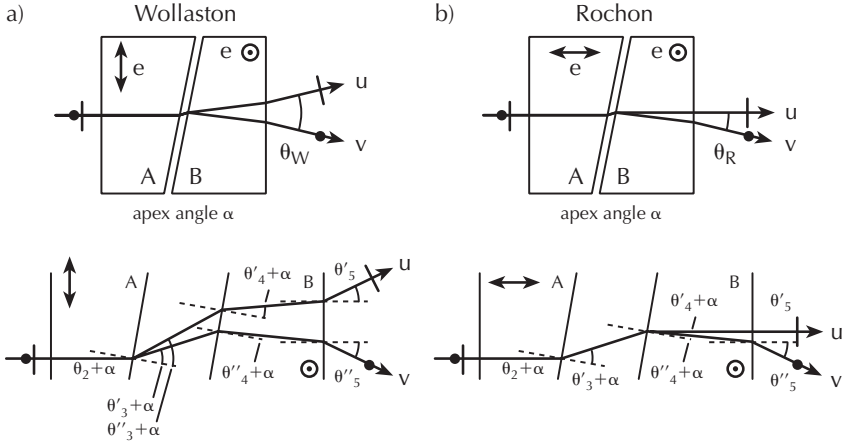

Fig. 4.28. Wollaston and Rochon compound prisms separate an input beam based on its polarization. The Wollaston prism symmetrically separates the orthogonal states while the Rochon prism deflects only the state aligned with the *e*-axis in prism B. Below shows ray-trace of orthogonal polarization components.

the u-beam following the u-path and the v-beam following the v-path. The output angles are calculated from Snell's equation applied to each interface. From left to right, the equations for the u-path are

$$\sin\theta_1 = n_e \sin\theta_2' \tag{4.7.3a}$$

$$n_e \sin(\theta_2' + \alpha) = n_g \sin(\theta_3' + \alpha) \tag{4.7.3b}$$

$$n_g \sin(\theta_3' + \alpha) = n_o \sin(\theta_4' + \alpha) \tag{4.7.3c}$$

$$n_o \sin\theta_4' = \sin\theta_5' \tag{4.7.3d}$$

where n_g is the index in the gap. For the v-path the equations are

$$\sin\theta_1 = n_o \sin\theta_2'' \tag{4.7.4a}$$

$$n_o \sin(\theta_2'' + \alpha) = n_g \sin(\theta_3'' + \alpha) \tag{4.7.4b}$$

$$n_g \sin(\theta_3'' + \alpha) = n_e \sin(\theta_4'' + \alpha) \tag{4.7.4c}$$

$$n_e \sin\theta_4'' = \sin\theta_5'' \tag{4.7.4d}$$

Taking incident angles as small but allowing the apex angle to be significant,[1] the two output deflections are related to the birefringence and apex angle as

$$\theta_5' - \theta_1 \simeq (n_e - n_o)\tan\alpha\,, \qquad \theta_5'' - \theta_1 \simeq -(n_e - n_o)\tan\alpha \tag{4.7.5}$$

The Wollaston deflection θ_W is the full angle between the outputs, which is

[1] The approximation is $\sin(\theta+\alpha) \simeq \theta\cos\alpha + \sin\alpha$.

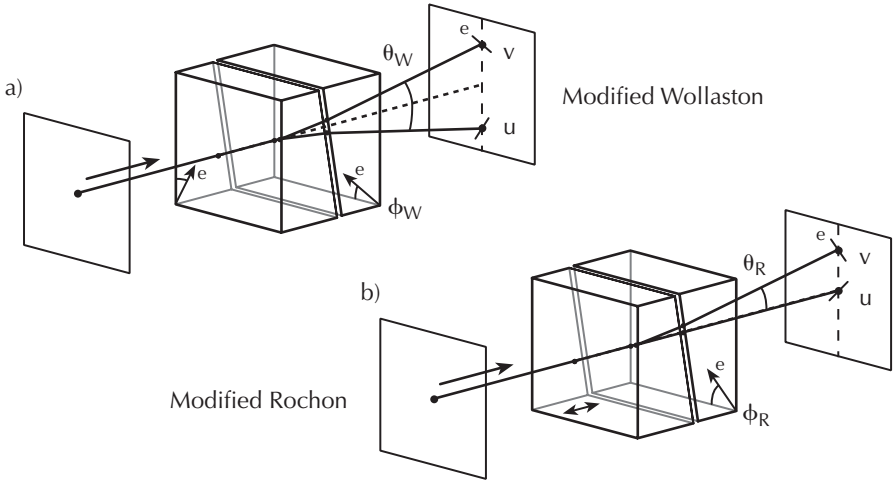

Fig. 4.29. Modified Wollaston and modified Rochon prisms. a) Modified Wollaston tilts the *e*-axes of the birefringent prisms while maintaining a 90° separation. The output polarization states are aligned to the *e*- and *o*-axes of the second prism. b) Modified Rochon prism tilts the *e*-axis of the second prism.

$$\theta_W = 2\,(n_e - n_o)\tan\alpha \tag{4.7.6}$$

As an example, to compensate for a 3° full-angle divergence between beams emergent from a dual-fiber collimator, using YVO_4 material which has a birefringence at 1.55 μm of $\Delta n = 0.2039$, the required apex angle is $\alpha \simeq 14.4°$.

The Rochon compound prism Fig. 4.28(b) is like the Wollaston in shape but the *e*-axis of prism A is oriented along the propagation axis. In this way both *u*- and *v*-path polarizations see the ordinary index and experience the same refraction into the gap. Moreover, in prism B the *u*-path also sees the ordinary index which in turn imparts zero net deflection. Only the *v*-path is deflected at the output. The Rochon deflection θ_R is the full angle between the outputs, which is

$$\theta_R = (n_e - n_o)\tan\alpha \tag{4.7.7}$$

The Rochon has half of the deflecting power of the Wollaston, but has the advantage of keeping one beam parallel to the input.

Path balancing is another key difference between the Wollaston and Rochon. For the Wollaston, in prism A the *u*-path has the extraordinary polarization while the *v*-path has the ordinary. In prism B these associations are reversed. As long as the prism lengths are the same the two paths are temporally balanced and one expects no appreciable PMD. In contrast, there is no temporal difference imparted by prism A of the Rochon, but there is by prism B. A single Rochon is not temporally balanced. The differential-group delays τ accumulated in the Wollaston and Rochon prisms are

$$\tau_W \simeq \frac{(n_e - n_o)(L_A - L_B)}{c} \tag{4.7.8a}$$

$$\tau_R \simeq \frac{(n_e - n_o)L_B}{c} \tag{4.7.8b}$$

where L_A and L_B are the lengths of the first and second prisms in each pair, and the small-angle limit is used. Using YVO_4 with a length $L_B = 2$ mm, the delay from a Rochon prism is $\tau \sim 1.3$ ps. This is an appreciable imbalance in the context of current component PMD specifications.

A variation of the Wollaston and Rochon compound prisms of significant practical importance is illustrated in Fig. 4.29 [56, 61]. The modified Wollaston compound prism changes the cut of the e-axes of prisms A and B while maintaining a 90° different between them. The modified Rochon compound prism changes the e-axis cut in prism B. The modified Wollaston and modified Rochon prisms impart the same polarization-dependent deflections as their standard counterparts, but the linear states of polarization are rotated to align with the ordinary and extraordinary axes in prism B. Tilting of the extraordinary axes in this way adds a degree of freedom in the polarization-evolution schemes used in isolators and circulators.

4.7.2 Kaifa Prism

The Kaifa prism is a hybrid of the Wollaston and Rochon prisms and is illustrated in Fig. 4.30 [2]. The Kaifa prism serves two functions at once: the displacement of one polarization from the other, and the deflection of the two polarizations. The prism can be designed with no differential-group delay.

The compound prism is made from two birefringent prisms. Unlike the preceding prisms, the extraordinary axis in prism A is cut at angle $\alpha_{\rm BC}$ to the longitudinal axis to produce Poynting vector walkoff along the u-path. For normal incidence, the k-vectors of the e- and o-rays remain coincident. At the hypotenuse interface the v-path follows the same path as in the Wollaston and Rochon prisms, while the u-path experiences a deflection that is between zero and $\theta_W/2$.

The Kaifa deflection θ_K is determined from ray tracing. The u-path follows

$$\sin\theta_1 = n_{\rm eff}\sin\theta_2' \tag{4.7.9a}$$

$$n_{\rm eff}\sin(\theta_2' + \alpha) = n_g \sin(\theta_3' + \alpha) \tag{4.7.9b}$$

$$n_g \sin(\theta_3' + \alpha) = n_o \sin(\theta_4' + \alpha) \tag{4.7.9c}$$

$$n_o \sin\theta_4' = \sin\theta_5' \tag{4.7.9d}$$

where $n_{\rm eff}$ is determined from the birefringence and extraordinary axis angle $\alpha_{\rm BC}$ (cf. (3.6.26) on page 117):

$$n_{\rm eff} = \frac{n_e n_o}{\sqrt{n_e^2\cos^2\alpha_{\rm BC} + n_o^2\cos^2\alpha_{\rm BC}}} \tag{4.7.10}$$

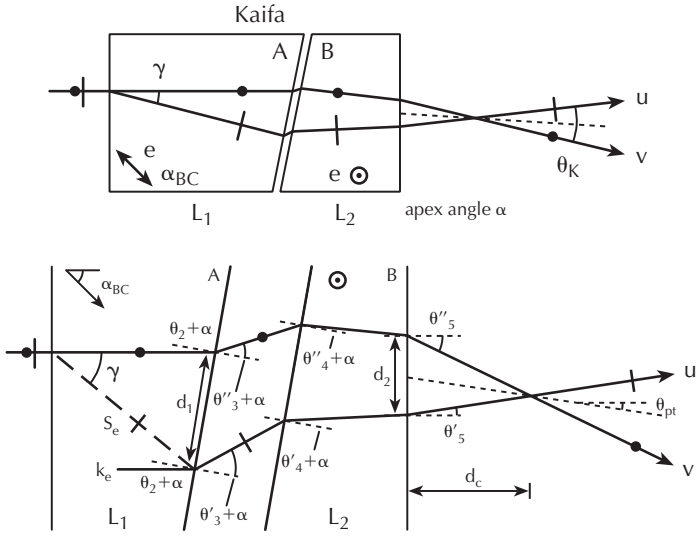

Fig. 4.30. The Kaifa prism is a hybrid of the Wollaston and Rochon prisms. Due to inclination of the extraordinary axis in prism A the Poynting vector of the extraordinary ray walks away from the ordinary ray. Prism B deflects both rays, but due to the intermediate refraction angle from prism A, the angle of the u-path output from prism B lies between that of the Wollaston and Rochon prisms.

Note that if the incident angle is not $\theta_1 = 0$ then (4.7.9a) must be replaced with (3.6.23) on page 115. For small incident angles, the deflection along the u-path is then

$$\theta'_5 - \theta_1 \simeq (n_{\text{eff}} - n_o) \tan\alpha \tag{4.7.11}$$

The v-path follows (4.7.4) with deflection (4.7.5). Accordingly, the Kaifa compound prism deflection angle is

$$\theta_K = (n_e + n_{\text{eff}} - 2n_o) \tan\alpha \tag{4.7.12}$$

The pointing direction, the center line of the two paths, is

$$\theta_{\text{pt}} = -\frac{1}{2}(n_e - n_{\text{eff}}) \tan\alpha \tag{4.7.13}$$

When $\alpha_{\text{BC}} = 0°$ the Kaifa prism reverts to a Rochon prism with $n_{\text{eff}} = n_o$. Likewise, when $\alpha_{\text{BC}} = 90°$ the prism reverts to a Wollaston prism with $n_{\text{eff}} = n_e$. In either of these two extremes there is no walkoff of the extraordinary path from the ordinary path.

The optical path lengths can be balanced in the Kaifa prism. The accumulated phase along the u- and v-paths is

$$\varphi_u = \frac{\omega}{c}\left(n_{\text{eff}} L_1 + n_o L_2\right) \tag{4.7.14a}$$

$$\varphi_v = \frac{\omega}{c}\left(n_o L_1 + n_e L_2\right) \tag{4.7.14b}$$

The requisite prism length ratio that balances the phase and thereby eliminates differential-group delay is

$$\frac{L_2}{L_1} = \frac{n_{\text{eff}} - n_o}{n_e - n_o} \tag{4.7.15}$$

The length L_1 of the first prism determines the displacement of the e-ray. The walkoff angle γ of the Poynting vector is governed by (cf. (3.6.15) on page 110)

$$\tan\gamma = -\frac{(n_e^2 - n_o^2)\sin\alpha_{\text{BC}}\cos\alpha_{\text{BC}}}{n_e^2\cos^2\alpha_{\text{BC}} + n_o^2\sin^2\alpha_{\text{BC}}} \tag{4.7.16}$$

The displacement d_1 at the end of prism A is

$$d_1 \simeq L_1 \tan\gamma \tag{4.7.17}$$

The change in displacement after transiting prism B is

$$(d_1 - d_2) \simeq L_2 \tan\left(\theta_4' - \theta_4''\right) \tag{4.7.18}$$

Given the displacement at the end face of prism B and the full deflection angle, the distance to the crossing point of the u- and v-paths is approximately

$$d_c \simeq \frac{d_2}{\theta_K} \tag{4.7.19}$$

Expansion of the respective terms yields

$$d_c \simeq \left(\frac{\tan\gamma - \left(\frac{n_{\text{eff}} - n_o}{n_e - n_o}\right)\left(\frac{n_{\text{eff}}}{n_o} - \frac{n_o}{n_e}\right)\tan\alpha}{(n_e + n_{\text{eff}} - 2n_o)\tan\alpha}\right) L_1 \tag{4.7.20}$$

The Kaifa prism is useful is some circulator as well as interleaver applications because of the simplicity of its displacement and deflection behavior.

4.7.3 Shirasaki Prism

The Shirasaki compound prism illustrated in Fig. 4.31 is a birefringent prism pair designed to split an input light ray into orthogonal polarization components that run parallel to one another [54, 57]. The birefringent prisms are designed such that one polarization component undergoes total internal reflection while at the same interface the remaining polarization component is transmitted through the Brewster angle. The Shirasaki prism is a variation on the Glan-Taylor prism but directs the outputs to run parallel.

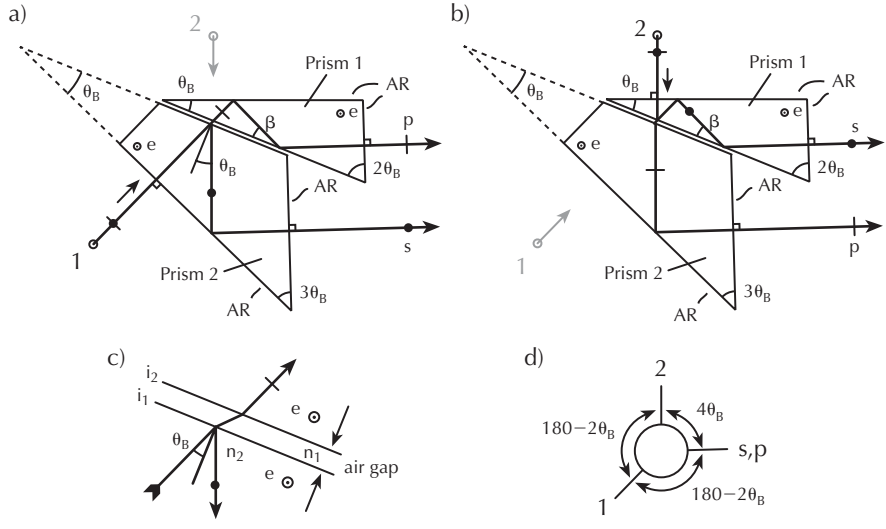

Fig. 4.31. The Shirasaki compound prism. Two birefringent prisms cut as illustrated separate a light beam into orthogonal linear components. At the air-gap interface between the two prisms one polarization is totally internally reflected while the other is transmitted through Brewster's angle. The extraordinary axis is aligned perpendicular to the page, and the output surfaces are AR coated. a) Input through port 1 separates polarizations onto two parallel paths, the p polarization runs along the top path. b) Input through port 2 also separates polarization, the p polarization runs along the bottom path. c) Optical path at air-gap interface. d) Angular orientation of four ports.

As illustrated in Fig. 4.31(a,b), there are four ports to the compound prism. Ports 1 and 2 have their polarization components resolved by the prism and diverted to run parallel at the output ports. Whether the p polarization component runs along the upper or lower output path depends on the input port, and likewise for the s polarization. The birefringent prisms have their extraordinary axes cut perpendicular to the plane in which the light travels. The compound prism is easily designed for positive uniaxial crystals.

The characteristic action of the compound prism lies at interface i_1 (Fig. 4.31(c)). Here one polarization component experiences total internal reflection, which is determined by the condition

$$n_2 \sin\theta_2 \geq n_1 \tag{4.7.21}$$

The other polarization is to experience total transmission through the Brewster angle. Recalling that the Brewster condition requires the reflected and refracted light to lie at right angles, or $\theta_1 + \theta_2 = \pi/2$, the reflection coefficient (3.5.39) on page 99 vanishes when

$$\tan\theta_2 = n_1/n_2 \tag{4.7.22}$$

With this condition satisfied, one writes $\theta_2 = \theta_B$, where here θ_B is the internal Brewster angle. For an isotropic material (4.7.21) and (4.7.22) cannot be simultaneously satisfied. However, they can be simultaneously satisfied for a uniaxial birefringent material. Consider, without loss of generality, a positive uniaxial material such that TIR occurs for the extraordinary index. In this case, the governing expressions are

$$n_e \sin\theta_2 \geq n_1 \tag{4.7.23a}$$

$$n_o \sin\theta_2 = n_1 \cos\theta_2 \tag{4.7.23b}$$

Combination of the square of these relations generates the condition that

$$n_e^2 - n_o^2 \geq n_1^2 \tag{4.7.24}$$

When the gap index is air, $n_1 = 1$ and (4.7.24) is satisfied. Rutile and YVO_4 satisfy this condition.

A consideration with this compound prism is the reflection coefficient when the prism index changes, as with temperature. With a temperature change, the input angle does not change but the index does. If one writes (3.5.39) as $\Gamma_{\rm TM} = f/g$, then to first order about the Brewster angle,

$$\frac{d\Gamma_{\rm TM}}{dn_2} \simeq \frac{df}{g} \tag{4.7.25}$$

Taking the differential and then substituting in Brewster's expression (4.7.22), reflectivity change from zero is

$$\frac{d\Gamma_{\rm TM}}{dn_2} \simeq \frac{(n_2/n_1)^2 - 1}{2n_2} \tag{4.7.26}$$

Consider that the prisms are made of YVO_4. At room temperature the reflection of the ordinary ray is zero. For a 40° temperature change, given a thermal-optic coefficient of $dn_o/dT \sim 8.6 \times 10^{-6}$, the reflection changes to $|\Gamma_{\rm TM}|^2 \sim -70$ dB. The Shirasaki prism was used to demonstrate a polarization-independent circulator having high extinction [35, 57].

Table 4.8. Summary of Waveplate Vector and Matrix Operators

Waveplate	Jones expressions	Stokes expressions
Quarter-wave		
$\{U, R\}$ Operators	$U_{\lambda/4} = \frac{1}{\sqrt{2}}(I - j(\hat{r} \cdot \vec{\sigma}))$	$R_{\lambda/4} = (\hat{r}\hat{r}\cdot) + (\hat{r}\times)$
$\{U, R\}_{\lambda/4}(\theta)$	$\frac{1}{\sqrt{2}} \begin{pmatrix} 1 - j\cos 2\theta & -j\sin 2\theta \\ -j\sin 2\theta & 1 + j\cos 2\theta \end{pmatrix}$	$\begin{pmatrix} \cos^2 2\theta & \sin 2\theta \cos 2\theta & \sin 2\theta \\ \sin 2\theta \cos 2\theta & \sin^2 2\theta & \cos 2\theta \\ -\sin 2\theta & \cos 2\theta & 0 \end{pmatrix}$
$\{U, R\}_{\lambda/4}(45^\circ)$	$\frac{1}{\sqrt{2}} \begin{pmatrix} 1 & -j \\ -j & 1 \end{pmatrix}$	$\begin{pmatrix} 0 & 0 & 1 \\ 0 & 1 & 0 \\ -1 & 0 & 0 \end{pmatrix}$
Half-wave		
$\{U, R\}$ Operators	$U_{\lambda/2} = -j(\hat{r} \cdot \vec{\sigma})$	$R_{\lambda/2} = 2(\hat{r}\hat{r}\cdot) - I$
$\{U, R\}_{\lambda/2}(\theta)$	$-j \begin{pmatrix} \cos 2\theta & \sin 2\theta \\ \sin 2\theta & -\cos 2\theta \end{pmatrix}$	$\begin{pmatrix} \cos 4\theta & \sin 4\theta & 0 \\ \sin 4\theta & -\cos 4\theta & 0 \\ 0 & 0 & -1 \end{pmatrix}$
$\{U, R\}_{\lambda/2}(45^\circ)$	$\frac{j}{\sqrt{2}} \begin{pmatrix} 0 & 1 \\ 1 & 0 \end{pmatrix}$	$\begin{pmatrix} -1 & 0 & 0 \\ 0 & 1 & 0 \\ 0 & 0 & -1 \end{pmatrix}$
Faraday rotator[a]		
$\{U, R\}$ Operators	$U_F = \cos\theta_F I \mp j\sigma_3 \sin\theta_F$	$R_F = \cos 2\theta_F + (1 - \cos 2\theta_F)(\sigma_3\sigma_3\cdot) \pm \sin 2\theta_F(\sigma_3\times)$
$\{U, R\}_F(\theta_F)$	$\begin{pmatrix} \cos\theta_F & \mp\sin\theta_F \\ \pm\sin\theta_F & \cos\theta_F \end{pmatrix}$	$\begin{pmatrix} \cos 2\theta_F & \mp\sin 2\theta_F & 0 \\ \pm\sin 2\theta_F & \cos 2\theta_F & 0 \\ 0 & 0 & 1 \end{pmatrix}$
$\{U, R\}_F(45^\circ)$	$\frac{1}{\sqrt{2}} \begin{pmatrix} 1 & \mp 1 \\ \pm 1 & 1 \end{pmatrix}$	$\frac{1}{\sqrt{2}} \begin{pmatrix} 1 & \mp 1 & 0 \\ \pm 1 & 1 & 0 \\ 0 & 0 & \sqrt{2} \end{pmatrix}$

[a] The (+) and (−) signs refer to the relation of the magnetization vector and Faraday rotation direction of the material. Once a sign is set, it is fixed for both forward and backward propagation.

References

1. M. Arii, N. Takeda, Y. Tagami, and K. Shirai, "Magneto-optic garnet," U.S. Patent 4,932,760, June 12, 1990.
2. V. Au-Yeung, Q.-D. Gao, and X. L. Wang, "Optical circulator," U.S. Patent 6,331,912, Dec. 18, 2001.
3. M. Bass, Ed., *Handbook of Optics: Volume II.* New York: McGraw-Hill, Inc., 1995.
4. J. M. Bennett, "A critical evaluation of rhomb-type quarterwave retarders," *Applied Optics*, vol. 9, pp. 2123–2129, 1970.
5. B. H. Billings, Ed., *Selected Papers on Polarization.* Bellingham, Washington: SPIE Optical Engineering Press, 1990, vol. MS 23, SPIE Milestone Series.
6. J. Bland-Hawthorn, W. V. Breugel, P. R. Gillingham, I. K. Baldry, and D. H. Jones, "A tunable lyot filter at prime focus: A method for tracing supercluster scales at z 1," *The Astrophysical Journal*, vol. 563, pp. 611–628, Dec. 2001.
7. C. D. Brandle, V. J. Fratello, and S. J. Licht, "Article comprising a magneto-optic material having low magnetic moment," U.S. Patent 5,608,570, Mar. 4, 1997.
8. C. F. Buhrer, "Four waveplate dual tuner for birefringent fitlers and multiplexers," *Applied Optics*, vol. 26, no. 17, pp. 3628–3632, 1987.
9. ——, "Quasi-achromatic optical isolators and circulators using prisms with total internal fresnel reflection," U.S. Patent 4,991,938, Feb. 12, 1991.
10. S. Cao, J. Chen, J. N. Damask, C. Doerr, L. Guiziou, G. Harvey, Y. Hibino, H. Li, S. Suzuki, K.-Y. Wu, and P. Xie, "Interleaver technology: Comparisons and applications requirements," *Journal of Lightwave Technology*, vol. 22, no. 1, pp. 281–289, Jan. 2004.
11. "Carpenter invar 36 alloy," Carpenter Technology Corporation, Wyomissing, Pennsylvania, 1990, edition date 08/01/1990.
12. "Kovar alloy," Carpenter Technology Corporation, Wyomissing, Pennsylvania, 1990, edition date 10/01/1990.
13. J.-H. Chen, K.-W. Chang, K. Tai, H.-W. Mao, and Y. Yin, "Apparatus capable of operating as interleaver/deinterleavers for filters," U.S. Patent 6,333,816, Dec. 25, 2001.
14. "Lithium niobate optical crystals," Crystal Technology, Inc., Palo Alta, CA, 1999. [Online]. Available: http://www.crystaltechnology.com/LN_Optical_Crystals.pdf
15. J. N. Damask, "Polarization mode dispersion generator," U.S. Patent 2002/0 012 487 A1, Jan. 31, 2002.
16. ——, "Composite birefringent crystal and filter," U.S. Patent 6,577,445, June 10, 2003.
17. J. N. Damask, P. R. Myers, G. J. Simer, and A. Boschi, "Methods to construct programmable PMD sources, Part II: Instrument demonstrations," *Journal of Lightwave Technology*, vol. 22, no. 4, pp. 1006–1013, Apr. 2004.
18. E. Desurvire, *Erbium-Doped Fiber Amplifiers, Principles and Applications.* Hoboken, New Jersey: Wiley-Interscience, 2002.
19. S. M. Etzel, A. H. Rose, and C. M. Wang, "Dispersion of the temperature dependence of the retardance in SiO_2 and MgF_2," *Applied Optics*, vol. 39, no. 31, pp. 5796–5800, Nov. 2000.
20. J. W. Evans, "The birefringent filter," *Journal of the Optical Society of America*, vol. 39, no. 3, pp. 229–242, 1949.

21. V. J. Fratello and R. Wolfe, *Handbook of Thin Film Devices, Vol. 4: Magnetic Thin Film Devices.* San Diego: Academic Press, 2001, ch. Epitaxial Garnet Films for Nonreciprocal Magneto-Optic Devices, pp. 93–141.
22. C. E. Gaebe, "Optical isolator and alignment method," U.S. Patent 5,737,349, Apr. 7, 1999.
23. D. J. Gauthier, P. Narum, and R. W. Boyd, "Simple, compact, high-performance permanent-magnet faraday isolator," *Optics Letters*, vol. 11, no. 10, pp. 623–625, 1986.
24. E. Hecht, *Optics*, 2nd ed. Reading, Massachusetts: Addison-Wesley Publishing Company, 1987.
25. A. J. Heiney and D. K. Wilson, "Optical isolators employing oppositely signed faraday rotating materials," U.S. Patent 5,087,984, Feb. 11, 1992.
26. F. Heismann, "Analysis of a reset-free polarization controller for fast automatic polarization stabilition in fiber-optic transmission systems," *Journal of Ligthwave Technology*, vol. 12, no. 4, pp. 690–699, Apr. 1994.
27. K. Hiramatsu, K. Shirai, and N. Takeda, "Low magnet-saturation bismuth-substituted rare-earth iron garnet single crystal film," U.S. Patent 6,031,654, Feb. 29, 2000.
28. "Hoya glass catalog," Hoya, Incorporated, 2004.
29. *Optical Interfaces for Multichannel Systems with Optical Amplifiers*, International Telecommunication Union Std. ITU-T G.692, Oct. 1998.
30. *Spectral Grids for WDM Applications: DWDM Frequency Grid*, International Telecommunication Union Std. ITU-T G.694.1, June 2002.
31. "PbMoO4 data sheet," Isomet Corporation, Springfield, Virginia, 2003. [Online]. Available: http://www.isomet.com/
32. "Casix product catalog 2003," JDSU, Inc., Canada, 2003. [Online]. Available: http://www.casix.com/crystals/birefringentcrystal.htm
33. D. Jones, S. Diddams, J. Ranka, A. Stentz, R. Windeler, J. Hall, and S. Cundiff, "Carrier-envelope phase control of femtosecond modelocked lasers and direct optical frequency synthesis," *Science*, vol. 288, pp. 635–639, 2000.
34. C. J. Koester, "Achromatic combinations of half-wave plates," *Journal of the Optical Society of America*, vol. 49(4), pp. 405–409, Apr. 1959.
35. H. Kuwahara, "Optical circulator," U.S. Patent 4,650,289, Mar. 17, 1987.
36. M. Legre, M. Wegmuller, and N. Gisin, "Investigation of the ratio between phase and group birefringence in optical single-mode fibers," *Journal of Lightwave Technology*, vol. 21, no. 12, pp. 3374–3378, Dec. 2003.
37. U. Morgner, R. Ell, G. Metzler, T. R. Schibli, F. X. Kartner, J. G. Fujimoto, H. A. Haus, and E. P. Ippen, "Nonlinear optics with phase-controlled pulses in the sub-two-cycle regime," *Physical Review Letters*, vol. 86, no. 24, pp. 5462–5465, 2001.
38. "Ohara glass catalog," Ohara, Incorporated, Kanagawa, Japan, 2004. [Online]. Available: http://www.oharacorp.com/swf/catalog.html
39. S. Pancharatnam, "Achromatic combinations of birefringent plates," *Proc. Indian Acad. Sci.*, vol. A41, pp. 137–144, 1955.
40. K. B. Rochford, A. H. Rose, and G. Day, "Magneto-optic sensors based on iron garnets," *IEEE Transactions on Magnetics*, vol. 32, no. 5, pp. 4113–4117, 1996.
41. K. B. Rochford, A. H. Rose, M. N. Deeter, and G. W. Day, "Faraday effect current sensor with improved sensitivity-bandwidth product," *Optics Letters*, vol. 19, no. 22, p. 1903, Nov. 1994.

42. K. B. Rochford, A. H. Rose, P. A. Williams, C. M. Wang, I. G. Clarke, P. D. Hale, and G. W. Day, "Design and performance of a stable linear retarder," *Applied Optics*, vol. 36, no. 26, pp. 6458–6465, Sept. 1997.
43. K. B. Rochford, A. Rose, M. Deeter, and G. Day, "Faraday effect current sensor with improved sensitivity-bandwidth product," in *Tenth Int'l Conference on Fiber Optic Sensors (SPIE 2360)*, B. Culshaw and J. Jones, Eds., Glasgow, Scotland, Oct. 1994, pp. 32–35.
44. "Optical glass description of properties," Schott Glass, Mainz, Germany, Sept. 2000, version 1.2. [Online]. Available: http://www.us.schott.com/sgt/english/products/catalogs.html
45. "Optical glass properties," Schott Glass, Mainz, Germany, Sept. 2000, version 1.2. [Online]. Available: http://www.us.schott.com/sgt/english/products/catalogs.html
46. "Synthetic fused silica," Schott Lithotec AG, Mainz, Germany, 2001. [Online]. Available: http://www.schott.com/lithotec/english/products/fused_silica.html
47. K. Shirai, K. Ishikura, and N. Takeda, "Bismuth-substituted rare earth iron garnet single crystal," U.S. Patent 5,565,131, Oct. 15, 1996.
48. ——, "Low saturated magnetic field bismuth-substituted rare earth iron garnet single crystal and its use," U.S. Patent 5,512,193, Aug. 30, 1996.
49. K. Shirai, M. Sumitani, N. Takeda, and M. Arii, "Optical isolator," U.S. Patent 5,278,853, Jan. 11, 1994.
50. K. Shirai, T. Takano, N. Takeda, and M. Arii, "Polarization-independent optical isolator," U.S. Patent 5,345,329, Sept. 6, 1994.
51. K. Shirai and N. Takeda, "Faraday rotator," U.S. Patent 5,535,046, July 9, 1996.
52. ——, "Bismuth-substituted rare earth iron garnet single crystal film," U.S. Patent 5,925,474, July 20, 1999.
53. K. Shirai, N. Takeda, and K. Hiramatsu, "Faraday rotator having a rectangular shaped hysteresis," U.S. Patent 5,898,516, Apr. 27, 1999.
54. M. Shirasaki, "Prism polarizer," U.S. Patent 4,392,722, July 12, 1983.
55. ——, "Polarization rotation compensator and optical isolator using the same," U.S. Patent 4,712,880, Dec. 15, 1987.
56. M. Shirasaki and K. Asama, "Compact optical islator for fibers using birefringent wedges," *Applied Optics*, vol. 21, no. 23, pp. 4296–4299, 1982.
57. M. Shirasaki, H. Kuwahara, and T. Obokata, "Compact polarization-independent optical circulator," *Applied Optics*, vol. 20, no. 15, pp. 2683–2687, Aug. 1981.
58. *Generic Reliability Assurance Requirements for Passive Optical Components*, Telcordia Technologies Std. GR-1221-CORE, 1999. [Online]. Available: http://telecom-info.telcordia.com/site-cgi/ido/index.html
59. S. Thaniyavarn, "Wavelength-independent polarization converter," U.S. Patent 4,691,984, Sept. 8, 1987.
60. G. R. Walker and N. G. Walker, "Polarization control for coherent communications," *Journal of Ligthwave Technology*, vol. 8, no. 3, pp. 438–458, Mar. 1990.
61. P. Xie and Y. Huang, "Compact polarization insensitive circulators with simplifed structure and low polarization mode dispersion," U.S. Patent 6,052,228, Apr. 18, 2000.